J. Appl. Comput. Mech., xx(x) (2026) 1-34
DOI: 10.22055/jacm.2026.49210.5807

ISSN: 2383-4536
jacm.scu.ac.ir

Shahid Chamran
University of Ahvaz

Journal of
Applied and Computational Mechanics

Research Paper

An Integrated CAD-MBD-FEM Framework for Virtual Prototyping of a New Foldable Mechanism for Deployable Propulsor Support in Urban Air Mobility Vehicles

Carlos Pérez Carrera[1], Rosario La Regina[2], Carmine Maria Pappalardo[3], Valentino Paolo Berardi[4], Domenico Guida[5]

[1]Department of Industrial Engineering, University of Salerno, Via Giovanni Paolo II, 132, 84084 Fisciano, Italy, Email: cperezcarrera@unisa.it
[2]Spin-Off MEID4 s.r.l., University of Salerno, Via Giovanni Paolo II, 132, 84084 Fisciano, Italy, Email: rlaregina@unisa.it
[3]Department of Industrial Engineering, University of Salerno, Via Giovanni Paolo II, 132, 84084 Fisciano, Italy, Email: cpappalardo@unisa.it
[4]Department of Industrial Engineering, University of Salerno, Via Giovanni Paolo II, 132, 84084 Fisciano, Italy, Email: vberardi@unisa.it
[5]Department of Industrial Engineering, University of Salerno, Via Giovanni Paolo II, 132, 84084 Fisciano, Italy, Email: guida@unisa.it

Received March 28 2026; Revised June 19 2026; Accepted for publication June 23 2026.
Corresponding author: Carmine Maria Pappalardo (cpappalardo@unisa.it)

Abstract. This paper presents a novel deployable mechanism for Urban Air Mobility (UAM) vehicles that supports propeller engines in flight and folds compactly for ground transport. To optimize this complex system, a rigorous Integration of Computer-Aided Design and Analysis (I-CAD-A) framework is developed in four sequential phases: 2D kinematic pre-dimensioning, detailed 3D geometric modeling, Multi-Body Dynamic (MBD) simulations to identify operational loads, and Finite Element Analysis (FEA) for structural verification. To bridge the critical data-transfer gap between dynamic MBD joint reactions and FEA structural boundaries, this study introduces and evaluates three novel load-transformation techniques: the Direct Reactions Method (DRM), the Moments Transformation Method (MTM), and the Loads Distribution Method (LDM). The proposed integrated approach yields a robust design for the foldable opening mechanism that supports propeller engines in autonomous urban air mobility vehicles, which serves as the paper's case study. In particular, the numerical experiments demonstrate that the proposed I-CAD-A framework yields a structurally sound, high-performance opening mechanism. Specifically, the proposed optimization process increased the minimum safety factor from the critical failure state of 0.22 to the standard value of 1.50, while incurring only a marginal mass penalty of 7.77%. Beyond the specific UAM application, this research provides a general, robust workflow for developing complex, articulated mechanical systems comprising rigid and flexible bodies. This research, therefore, not only proposes a new design for a foldable opening mechanism but also offers a detailed, structured, and robust methodology for developing complex mechanical systems composed of articulated rigid-flexible bodies.

Keywords: Theoretical and Applied Mechanics, Mechanics of Machines, Integration of Computer-Aided Design and Analysis (I-CAD-A), Computer-Aided Design (CAD), Multi-Body Dynamics (MBD), Finite Element Analysis (FEA), Urban Air Mobility (UAM).

1. Introduction

1.1 General Perspective and Main Motivations

Flying cars and self-driving technology are important research areas that represent a frontier in sustainable and safe mobility. A system that combines these two technologies can decrease traffic, lower emissions, improve safety, and reduce the risk of accidents [1–4]. In recent years, advances in technology, engineering, and materials science have made this vision more concrete. The increasing demand for urban mobility solutions and rising road congestion has led to a growing interest in personal aerial vehicles that can operate both on the ground and in the air [5–9]. The advent of flying cars is perceived as a potential solution to traffic congestion in densely populated areas, offering a more expedient and flexible mode of transportation [10–13]. Nevertheless, this novel mode of transportation presents a unique set of engineering challenges that must be addressed to guarantee the safety, dependability, and practicality of these vehicles [14–16]. Among the numerous challenges inherent to the development of flying cars, the design of propeller-folding mechanisms represents a particularly crucial aspect [17]. The ability of flying cars to transition between ground and air modes is enabled by propeller-folding mechanisms that fold the propellers during ground operation and deploy them for flight. The structural integrity of the propeller-folding mechanism is of paramount importance for the safe operation of flying cars, as any failure in this system could result in catastrophic consequences during flight or while transitioning between modes [18–21].

The significance of propeller-folding mechanisms extends beyond the specific context of flying cars. Similar mechanisms are employed in a variety of aerospace applications, including commercial and military aircraft, where spatial limitations necessitate folding propellers to accommodate storage within confined spaces, such as hangars or aircraft carriers [22–24]. In all of these cases, the mechanical system must be capable of withstanding substantial forces and moments due to external and internal excitation.

Accordingly, the insights derived from this study may have broader applications in the field of aviation, extending beyond the domain of personal aerial vehicles.

The structural components analyzed in the present study include the most critical components, that is, the pins that connect the various elements of the folding mechanism and the arm that transmits forces from the propeller to the vehicle body. These components are subjected to a multitude of complex loads during operation, including bending moments, shear forces, and axial loads [25–28]. Consequently, it is essential to ensure the strength and durability of these components, as they are instrumental to maintaining the overall structural integrity of the propeller-folding mechanism. The failure of these components could result in a loss of vehicle stability and safety, both on the ground and in flight [29, 30]. Therefore, a rigorous design methodology is fundamental. The goal is to analyze the mechanical behavior of components while accounting for all possible stresses acting on the system. To ensure the integrity and durability of the mechanism, it is necessary to precisely describe the entire force field and evaluate the effects these generate on the overall assembly. In this sense, integrating multibody analysis with the finite element method provides a comprehensive and realistic view of the system behavior [31, 32].

In the context of designing and analyzing complex articulated mechanisms, the integration of computer-aided design, multibody dynamics, and the finite element method has become a widely adopted methodology due to its capacity to streamline the design process and enhance the structural analysis of systems with multiple interacting components [33, 34]. This hybrid approach allows engineers to simulate the behavior of mechanical systems at various stages, from geometric modeling to the assessment of dynamic performance and stress distribution under different load conditions [35, 36]. In this vein, the folding propeller mechanisms of flying cars represent a distinctive and intricate system that can benefit from a comprehensive design approach, given the interdependence of structural, aerodynamic, and mechanical considerations. Thus, this is the comprehensive background in which this investigation is conducted, thereby fulfilling the primary motivations mentioned above.

1.2 Literature Review

A synthetic literature survey pertinent to the topics of interest for this investigation is provided below.

The advent of flying cars is poised to revolutionize transportation, offering a new level of convenience and flexibility for personal travel [11, 37]. Nevertheless, for these vehicles to become a practical reality, they must comply with the rigorous safety and performance standards that will undoubtedly be set forth [38, 39]. It is, indeed, clear that creating vehicles capable of operating on both the ground and in the air requires a new design approach. Starting from a detailed Computer-Aided Design (CAD) model, multibody simulation allows for the definition of realistic kinematic and dynamic scenarios of engineering interest, from which the most critical load conditions are derived [40, 41]. To this end, developing a high-fidelity Multi-Body Dynamic (MBD) model represents a fundamental step in the design process analyzed in this work. Subsequently, by applying the loads resulting from the multibody analysis to a structural model constructed using the Finite Element Method (FEM), it is possible to investigate stress distributions, deformations, and localized stresses, and to verify the structural integrity of the most solicited components. This integrated approach enables validation of system geometry and robustness by effectively combining CAD, MBD, and FEM models. For instance, the combination of MBD and FEM models allows for identification of the forces acting on components and their distribution across materials, thereby providing valuable insights into potential failure modes [42, 43]. This dual approach is of paramount importance for ensuring the safety and reliability of flying cars, where even minor design flaws can have significant consequences for safety and vehicle performance.

Computer-Aided Design (CAD) is a pivotal tool in contemporary engineering, providing a platform for the creation, modification, and analysis of three-dimensional models of mechanical systems [44, 45]. Historically, CAD has evolved from a tool used primarily for drafting and geometric modeling to an indispensable component of the product design and engineering process [46, 47]. In recent decades, significant advances in CAD technology have facilitated the creation of highly detailed models, which serve as the basis for subsequent analysis. The aforementioned models provide the requisite geometric data for simulations to be performed in Multi-Body Dynamics (MBD) and Finite Element Method (FEM) environments. More specifically, the integration of CAD into the analysis of mechanical systems has been a topic of extensive exploration in recent literature. Pérez Bayas et al. posited that CAD models facilitate not only the initial design process but also iterative testing and refinement when integrated with other analytical tools [48].

In the context of flying cars, CAD software is instrumental for modeling the articulated mechanisms that fold and deploy the propellers, where precise control over the geometry is paramount. Computer-aided design ensures the accurate representation and subsequent analysis of complex shapes, such as those of the propeller arms and pins, in downstream processes. Moreover, the precision of the CAD model is directly proportional to the fidelity of both dynamic and structural simulations [49]. In [50], Louhichi et al. highlight the importance of CAD precision, underscoring that minor discrepancies in the geometric model can lead to significant differences in subsequent MBD and FEM analyses. For folding propeller mechanisms, it is therefore essential to model the pins, arms, and joints with high precision to ensure the correct transfer of loads and the reliable operation of the system in both ground and air modes. Additionally, CAD enables the expeditious fabrication of prototypes, thereby enabling designers to evaluate disparate configurations and optimize the mechanism before commencing physical testing [51].

Multi-Body Dynamics (MBD) provides a framework for analyzing the motion and interactions of interconnected rigid and flexible bodies within a mechanical system [52–55]. The utility of MBD in analyzing articulated systems has been well documented in the literature. In the context of flying cars, MBD is paramount for understanding the dynamic forces and moments generated by the propeller-folding mechanism during both deployment and retraction. The MBD approach enables simulation of the entire mechanism operations, incorporating the forces acting on the joints and links as the vehicle transitions between flight and ground modes. For example, Dietz et al. illustrated the use of MBD to determine dynamic loads in railway components, subsequently transferring these loads to FEM for further structural analysis [56]. Similarly, Braccesi et al. underscored the benefits of employing MBD to simulate intricate mechanical systems and ascertain the reaction forces that shape stress distributions within the system [57].

The workflow discussed earlier is directly applicable to the design of flying cars, where MBD can be used to predict load distributions and component interactions, including propeller arms, pins, and actuators, during the propeller-folding process. In the case of folding propellers, MBD simulations help identify critical areas where high stress concentrations or mechanical instabilities may occur, thereby informing the FEM analysis. Software such as MSC ADAMS is frequently used for these simulations, enabling engineers to model both rigid and flexible bodies within the system [58]. The application of MBD enables the simulation of the complete range of motions that the folding propeller mechanism will undergo during operation, including articulated and constrained mechanical systems subjected to friction forces [59], encompassing both static ground conditions and dynamic flight maneuvers [60]. Such capabilities are essential to ensuring the mechanism withstands the forces generated across all operational scenarios without excessive wear or failure.

The Finite Element Method (FEM) is a widely used technique for structural analysis, particularly for complex geometries and varying load conditions where analytical solutions are not feasible [61, 62]. By dividing a structure into discrete components, the FEM numerical approach enables engineers to assess the distribution of stress, strain, and displacement across the entire system. In the CAD-MBD-FEM workflow, the FEM application represents the final step in assessing the ability of the propeller-folding mechanism to withstand the loads and stresses identified in the MBD simulation. The work of Akgun et al. highlights the significance of FEM in mechanical design, particularly in the context of systems comprising articulated mechanisms [63]. In another case study analyzed by Pappalardo et al. [64], the authors employed the multibody dynamics approach to assess the reliability of scissor-lift mechanisms by analyzing the dynamic behavior of the key mechanical components. This methodology is highly relevant to the folding propeller mechanisms of flying cars. Similarly, Louhichi et al. propose that integrating FEM with CAD and MBD enables iterative design refinement, in which stress analysis results inform the geometric model for further optimization [65].

Another challenge in this integration is modeling flexible components in MBD simulations, as traditional MBD tools are better suited to rigid-body dynamics. In [66], Hamed et al. proposed that incorporating supplementary degrees of freedom to accommodate deformation modes could enhance the precision of these simulations. This is particularly pertinent to the folding propeller mechanism, in which specific components may undergo both rigid-body motion and elastic deformation during operation. Additionally, integrating flexible bodies into the MBD model enables engineers to achieve a more accurate representation of the resulting dynamic behavior. In [67], Sun et al. demonstrated the effectiveness of the finite element method in designing a flying car chassis. This method enabled the development of a strong but lightweight structure. In [68], De Simone et al. proposed an advanced design approach for the optimization of a vertical take-off vehicle, using an approach based on the Design of Experiments (DOE) technique, applied to a parametric model developed in the SIMSCAPE MULTIBODY simulation environment. The optimal configuration was then validated using an FEM model, enabling evaluation of the kinematic and dynamic behavior of this mechanism.

To conclude, the consistent body of literature discussed above testifies to the importance of the main topics addressed and solved in this study.

1.3 Formulation of the Principal Research Questions of this Study

In mechanical and industrial engineering problems, designers use CAD (Computer-Aided Design) software that employs NURBS (Non-Uniform Rational B-splines). NURBS enable the generation of smooth, elegant curves and surfaces, ensuring optimal representation of parts. Analysts, however, must transform these elegant but computationally inefficient representations into finite elements to perform structural analyses using the FEM (Finite Element Method) [69, 70]. Finite element analysis and CAD are multi-billion-dollar sectors, yet they do not truly interact. According to a 1999 study by the National Institute of Standards and Technology, the lack of integration between CAD and analysis cost the U.S. automotive industry more than 600 million dollars per year [71]. Indeed, it has been estimated that 60% of the total time required to carry out the analysis is spent converting the CAD model into one suitable for FEA (Finite Element Analysis) [72]. This stage entails simplifying the complete CAD model to remove all components not required for subsequent analyses, as well as identifying and correcting potential geometric issues [73, 74]. The simplified model must then be appropriately transferred to the analysis software, within which all connections among the various parts must be defined.

The 'pre-processing' stage constitutes the actual bottleneck of the entire workflow described above, yet it is essential to reduce computational time as much as possible [75]. Automating these phases would save time and, therefore, enable analysis results to be obtained more rapidly. In this way, more analyses could be performed, and development could be pushed toward increasingly complex and safer products. By contrast, 20% of the time is devoted to mesh generation and the subsequent manipulation stage. This phase is essential because the element size must be selected to avoid making the model computationally burdensome while preventing the analysis results from deviating too far from reality. The remaining 20% of the time is used for analysis, including defining boundary and loading conditions and performing the solution phase of the mathematical model. Precisely because of this difficulty, complex and innovative components are being designed less and less frequently. The approximately 80/20 modeling/analysis ratio is, therefore, a widespread industrial problem. There is a strong desire to reverse this trend; however, despite substantial efforts, the progress achieved has been limited. The primary issue is the lack of integration between CAD and FEA, which researchers are addressing by developing I-CAD-A (Integration of Computer-Aided Design and Analysis) environments [76, 77].

The integration of CAD, MBD, and FEM software has been widely acknowledged as a practical methodology for optimizing complex mechanical systems. CAD models provide the geometric foundation, MBD simulations offer insight into the dynamic loads and interactions within the system, and FEM assesses the structural integrity of the components. This integrated approach not only improves the efficiency of the design process but also enhances the accuracy of the final product. In [78], Perez Bayas et al. highlight that integrating these tools enables a unified workflow that spans from initial geometric design to dynamic and structural analysis. Braccesi et al. identified one of the principal challenges in integrating CAD, MBD, and FEM as the efficient communication between software platforms [79]. To address this issue, they proposed a methodology in which the FEM mesh is generated directly from the CAD model, obviating the need for additional simplifications. This reduces the time required to prepare the model for analysis and minimizes the potential for errors during data transfer. This streamlined approach is particularly advantageous for applications such as folding propeller mechanisms, where both dynamic and structural performance are of paramount importance.

Despite the clear advantages of these integrated environments, fully automating the design-analysis-redesign loop remains a significant challenge and a primary focus of ongoing research. Implementing automated optimization algorithms, such as genetic algorithms or gradient-based optimizers, to directly link MBD transient outputs to CAD parametric dimensions is often hindered by geometric robustness and numerical stability issues during automated feature regeneration. The field still lacks standardized data interoperability protocols that can handle the nonlinearities of complex deployable mechanisms without human intervention. This complexity is further compounded by the uncertainties inherent in the design of high-performance mechanical systems, which necessitate a cautious approach to automation to avoid propagating modeling errors [80]. However, effective methodologies for integrated CAD-MBD-FEM analysis have been proposed in the literature, forming the basis of the present research [35]. This study, in particular, focuses on developing a validated, high-fidelity manual iterative framework as a critical prerequisite. This baseline is essential to ensure that the sensitivity of the foldable mechanism is fully understood before transitioning to fully automated optimization loops in subsequent development phases.

1.4 Scope and Contributions of this Investigation

A new class of vehicles is emerging and defining a new type of personal and urban transportation. These vehicles, called flying cars, are playing a leading role in the development of Urban Air Mobility (UAM). The aim is to develop vehicles that are capable of both ground and air transportation. This makes it possible to decrease vehicular traffic and reduce emissions. Given the dual application, it is necessary to achieve a strong, lightweight structure. From this perspective, this research proposes the design of a deployable opening mechanism capable of supporting the engines of a flying car and, at the same time, folding during ground transport, reducing the overall size of the resulting multifunctional vehicle.

The development of flying cars represents one of the most exciting challenges of modern engineering, with the potential to revolutionize both urban mobility and personal transportation [81]. In this vein, the folding and deployment mechanisms for propellers are critical, particularly during transitions between ground and air modes. The principal objective of this investigation is, therefore, to design a mechanism for this particular application, with a focus on the structural integrity of the pins and the arm. Given the structural role these components play in ensuring the reliability of the opening mechanism, a comprehensive design methodology is needed to guarantee their performance under diverse load conditions.

In the context of the present research, the use of advanced design and modeling techniques is essential. The design phases can be divided into four macro-categories that iteratively follow each other: a) preliminary sizing with the Euler-Bernoulli beam theory; b) geometric modeling based on CAD software; c) kinematic and dynamic modeling through MBD software; and d) strength analysis using FEM software. This comprehensive analysis concentrates on the pivots of the mechanism, which not only support the structure but also enable the rotation and movement required during deployment. The arm supporting the propulsion system of the vehicle plays an equally important role. In particular, both components must be modeled and analyzed in detail to ensure the system remains intact under operational stress.

To break down the barriers between engineering design and analysis, it is necessary to reconstruct the entire process while maintaining compatibility with existing techniques. A fundamental step is to focus on a single geometric model that can be used directly as an analysis model or from which the analysis models can be derived automatically. This will require replacing the traditional finite element representation with an analysis procedure based on the CAD representation. In this way, it will also be possible to address the discrepancy between the geometric and analysis models [82]. This discrepancy often makes simulations difficult and inefficient, especially when design parameters and the associated geometry must be repeatedly modified and updated [83]. The lack of integration also renders optimization processes very slow and inefficient [84]. It is often necessary to solve an optimization problem, such as minimizing a function subject to equality and inequality constraints [85]. To do so, the design-analysis-redesign phases shown in Figure 1 must be carried out entirely manually.

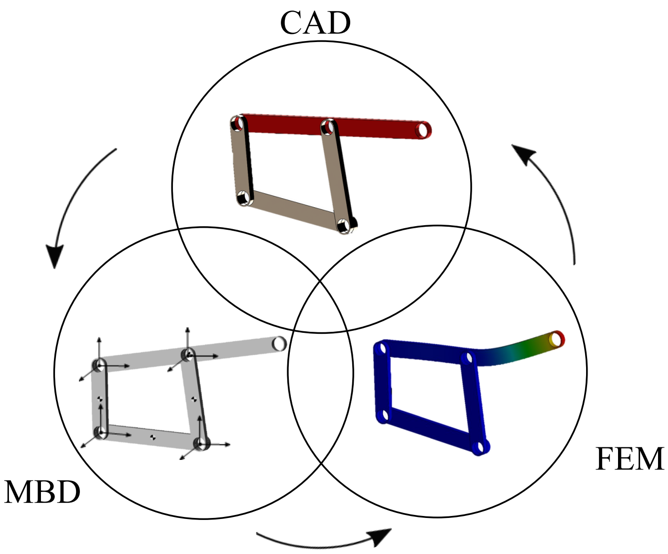

Fig. 1. Challenges in the manual integration of CAD, MBD, and FEM computational methodologies.

One of the principal challenges in this study is accurately translating reaction forces and moments from the MBD model into the FEM analysis. Despite the widespread use of integrated CAE environments, the current literature lacks a detailed, standardized protocol for mapping transient dynamic reactions onto static structural meshes. While many studies use the general CAD-MBD-FEM sequence, they often omit the specific mathematical or physical criteria that bridge these disparate simulation domains, treating load transfer as a trivial secondary step. Furthermore, common commercial solutions typically rely on internal, flexible-body solvers that employ automated model reduction. However, these black-box approaches often obscure the underlying load-distribution mechanics at the joint level and limit the designer's control over interface behavior.

To address and resolve the issues mentioned above, the performance of three different approaches is examined in this investigation: 1) the Direct Reactions Method (DRM), 2) the Moments Transformation Method (MTM), and 3) the Loads Distribution Method (LDM). These innovative approaches represent three novel methods specifically devised in this investigation. Thus, to effectively address the main issues considered in this study, three methodologies are proposed and distinguished, with a view to understanding which best represents actual behavior from a stress-and-strain perspective. The comparative analysis presented in the paper demonstrates how incorrect load assessments can lead to faulty system design. Furthermore, the Loads Distribution Method (LDM), in which loads were applied as surface pressures across the pins, was identified as the most realistic simulation technique. This approach reduced stress concentrations and provided a more accurate representation of the mechanical behavior of each structural component. This methodology was employed for the final analysis of the pins and the arm, ensuring that all elements could withstand the operational loads.

This study presents the design of a deployable opening mechanism that supports the engines attached to the propellers of a flying car and folds during ground transport, thereby reducing the overall size of the final vehicle prototype. To ensure the structural integrity of the resulting design, which is the most fundamental feature of the proposed design, all components are assumed to be made of metallic materials. An interesting direction for future work could be to fabricate the supporting arm from composite materials to reduce the weight of the mobile parts of the articulated system, while keeping the deployment system metallic to maintain overall structural strength. Thus, in a future extension of the research, the connection between the two components will be studied as a glued joint using cohesive models [86–88].

It is important to emphasize that the methodology presented herein is centered on virtual prototyping, a strategic paradigm shift in aerospace engineering that aims to validate complex kinematic architectures before allocating manufacturing resources. Using a high-fidelity, integrated CAD-MBD-FEM environment, the design space is explored and structural risks are mitigated cost-effectively, thereby addressing the current lack of comparative benchmarking for existing electric Vertical Take-Off and Landing (eVTOL) foldable mechanisms. However, this is a direct consequence of the Urban Air Mobility sector's technological maturity. At present, the vast majority of academic research focuses on operational aspects such as acoustic signatures, urban integration, and communication infrastructure. At the same time, the structural and mechanical details of commercial prototypes are strictly protected by corporate confidentiality. As this technology transitions from conceptual development to certification, the public availability of such data is expected to increase. In this context, the present study establishes a necessary numerical baseline for the subsequent phase of the project, which involves constructing physical demonstrators. These functional prototypes will provide the experimental validation and empirical correlation required to finalize the design for flight testing, effectively bridging the gap between the digital twin and the physical aerospace component.

As explained above, this subsection concisely summarizes the broad scope and the main contributions of the present investigation, which are discussed in detail throughout the paper. In summary, the main original contributions of this work are as follows: (I) the development of a complete CAD-MBD-FEM workflow for the virtual prototyping of a deployable propulsor-support mechanism; (II) the formulation and comparison of three load-transfer strategies for mapping MBD joint reactions into FEM boundary/loading conditions; (III) the identification of the Loads Distribution Method as the most physically representative approach for pin verification; and (IV) the iterative structural redesign of the critical pins and support arm until the prescribed safety-factor requirement is achieved.

1.5 Organization of the Manuscript

In addition to Section 1., which serves as an introduction to this work, this paper is organized as follows. Section 2. lays the foundation for the background material and describes the computational methods used, which together define the proposed integrated methodological approach that leads to a combined CAD-MBD-FEM technique. Section 3. defines the central concept of the present design and describes the key elements to be addressed and verified with subsequent analysis. Section 4. provides a clear presentation of the numerical results obtained in this research across the different environments and is entirely dedicated to the discussion of the final results from the implementation of the proposed CAD-MBD-FEM methodology. Finally, Section 5. provides a summary of the findings of this work, the main conclusions, and an outlook on future research directions for the design and optimization of articulated mechanisms using the integrated CAD-CAE methodology proposed herein.

2. Background Materials, Computational Methods, and Proposed Approach

2.1 Perspective on Computer-Aided Engineering (CAE)

This section provides an overview of the background materials and computational methods used in this investigation, with special attention to the fundamental issues encountered in modern Computer-Aided Engineering (CAE) design and synthesis problems. In particular, the discussion below focuses on the Integration of Computer-Aided Design and Analysis (I-CAD-A). This advanced approach synergistically integrates apparently incompatible tools from Computer-Aided Design (CAD), Multibody System Dynamics (MSD), and Finite Element Analysis (FEA). Some general perspectives on this problem are presented herein, while the subsequent parts of this section summarize the typical features of the mathematical approaches that underlie Computer-Aided Design (CAD), Multibody System Dynamics (MSD), and Finite Element Analysis (FEA). In addition, the last part of this section presents the approach adopted throughout this study to achieve the desired Integration of Computer-Aided Design and Analysis (I-CAD-A).

Furthermore, this section establishes the integrated theoretical foundation required to navigate the multidisciplinary complexity inherent in the design and validation of deployable propulsor support systems. To enable a rigorous transition from conceptual modeling to high-fidelity virtual prototyping, it is essential to delineate the fundamental principles of CAE, CAD, MBD, and FEM as they pertain specifically to this aerospace application. The following subsections provide a structured roadmap of the methodological pipeline, beginning with a precise geometric definition in a CAD environment and progressing to multibody dynamics needed to capture the complex mechanism's dynamic response. This is ultimately coupled with advanced finite element methods to assess structural integrity under rigorous operational loads. By providing this theoretical background at the outset, the manuscript ensures that the reader possesses the necessary conceptual tools to appreciate the sophisticated synergy required for the successful development of the complex deployable systems presented in the subsequent research results.

In recent years, Computer-Aided Engineering (CAE) has become a cornerstone of structural design, allowing for systematic exploration and optimization of complex mechanical systems [89]. Despite these advances, contemporary workflows remain fundamentally constrained by the interplay among high-fidelity simulation, design representation, and optimization in the presence of strongly nonlinear structural responses. In structural optimization, nonlinear behavior undermines the effectiveness of classical optimization strategies. Although adjoint formulations offer theoretical efficiency for large-scale sensitivity analysis, their robust implementation remains challenging for nonlinear transient problems with discontinuous updates, evolving damage, and component optimization. Another persistent methodological limitation lies in design parameterization. Topology and shape optimization depend critically on the representation of geometry and material distribution. These limitations indicate that advances in computer-aided engineering are challenged not only by computational cost but also by deeper methodological issues, including nonlinear model complexity, numerical sensitivity, optimization tractability, and representational fidelity. Most of all, a fundamental issue is the incompatibility between the mathematical formulations that characterize the computational environments used for geometric design, kinematic and dynamic analysis, and structural strength verification.

In modern mechanical engineering, the Integration of Computer-Aided Design and Analysis (I-CAD-A) is severely limited by incompatibilities arising from different computational representations and numerical requirements across Computer-Aided Design (CAD), Multibody System Dynamics (MSD), and Finite Element Analysis (FEA). In general, CAD systems primarily use boundary representations and parametric, feature-based models built with trimmed NURBS surfaces and topological entities. These models are designed to preserve the original design intent rather than to focus on computational stability. In contrast, MSD solvers typically require precise, robust geometric descriptions that are well-defined and suitable for both rigid-body dynamics and flexible-body formulations. Small gaps, component overlaps, redundant features, and ambiguous contact surfaces generated by CAD kernels can destabilize constraint enforcement, contact detection, and numerical integration. Furthermore, FEA introduces an additional layer of incompatibility because it depends on meshable solid domains and well-conditioned discretizations. Also, CAD models frequently exhibit non-manifold edges, sliver faces, small radii, and geometric degeneration that obstruct automated meshing and degrade element quality, leading to ill-conditioned stiffness matrices and convergence failures. Moreover, translating CAD geometry via neutral formats, e.g., STEP or IGES, often results in the loss of parametric constraints, tolerance inconsistencies, and corrupted topology, which propagate differently through the MSD and FEA preprocessing pipelines. This incompatibility is exacerbated when flexible multibody dynamics are sought, since mapping between CAD-based geometry, FEA-derived reduced-order models, and MSD-compatible body representations requires consistent reference frames, material metadata, and interface definitions that are not natively supported across tools. Consequently, I-CAD-A workflows remain sensitive to geometric fidelity, kernel-dependent tolerances, and incompatible abstraction levels, requiring extensive manual healing, defeaturing, and reconciliation to achieve robust interoperability.

2.2 Overview of Computer-Aided Design (CAD)

In mechanical engineering, CAD software is a tool used for solid modeling and geometrically representing objects with complex three-dimensional shapes. This approach is indeed used in various fields, both engineering and non-engineering. A CAD tool allows for precise modeling of the geometry of components that form a mechanical system, thereby creating an assembly, checking for interference, and verifying the manufacturability of the virtual prototype devised for a new product. For these reasons, CAD modeling plays a fundamental role in the modern mechanical engineering industry.

To accurately represent a three-dimensional object, CAD programs mainly use a mathematical representation based on the Non-Uniform Rational B-spline (NURBS) [90]. For the sake of demonstration, consider a space of dimension $d = 3$. From a mathematical point of view, the parametric equations of a curve described by a vector $\boldsymbol{C}(u)$ of dimensions $d \times 1$ based on the NURBS representation are reported below:

$$\boldsymbol{C}(u) = \sum_{i=1}^{k} R_i(u)\,\boldsymbol{P}_i \tag{1}$$

being:

$$R_i(u) = \frac{w_i N_{i,n}(u)}{\sum\limits_{p=1}^{k} w_p N_{p,n}(u)} \tag{2}$$

where u is the curve intrinsic parameter, i is an integer index, $\boldsymbol{P}_i$ are the control points of the parametric curve $\boldsymbol{C}(u)$, w_i are the weights associated with the control points, $N_{i,n}(u)$ are the B-spline basis functions having degree n, and k is the number of knots along the curve direction. The control points represent geometric coefficients of the curve, which, together with the weights, the basis functions, and the knot vector that governs their parameterization and range of influence, determine the three-dimensional shape of the curve. Basically, the curve is a linear combination of the rational basis functions, in which the basis functions in u define the variation along the intrinsic curve direction.

On the other hand, the parametric equations of a NURBS surface described by a vector $\boldsymbol{S}(u, v)$ of dimensions $d \times 1$ can be obtained as the tensor product of two NURBS curves. By doing so, using two independent control parameters u and v, which are respectively associated with subscripts i and j, it is possible to get the following formulation:

$$\boldsymbol{S}(u, v) = \sum_{i=1}^{k} \sum_{j=1}^{l} R_{i,j}(u, v)\boldsymbol{P}_{i,j} \tag{3}$$

being:

$$R_{i,j}(u, v) = \frac{w_{i,j} N_{i,n}(u) N_{j,m}(v)}{\sum\limits_{p=1}^{k} \sum\limits_{q=1}^{l} w_{p,q} N_{p,n}(u) N_{q,m}(v)} \tag{4}$$

where u and v are the surface intrinsic parameters, i and j are integer indexes, $\boldsymbol{P}_{i,j}$ are the control points of the parametric surface $\boldsymbol{S}(u, v)$, $w_{i,j}$ are the weights associated with the control points, $N_{i,n}(u)$ and $N_{j,m}(v)$ are the B-spline basis functions having respectively degree n and m, and k and l are the number of knots along the two surface directions. Thus, the surface is a bilinear combination of the rational basis functions in the two directions, in which the basis functions in u define the variation along one intrinsic surface direction, while those in v define the variation in another intrinsic surface direction.

In summary, NURBS form a unified mathematical framework for representing and manipulating parametric curves and surfaces with high geometric fidelity. They generalize polynomial B-splines by incorporating rational weighting, enabling the exact representation of conic sections and quadratic geometries while retaining the locality, smoothness control, and numerical stability of spline bases. A NURBS entity is defined over a non-uniform knot vector and a set of weighted control points, whose blending functions determine the shape and continuity. This formulation supports efficient refinement, stable evaluation, and precise continuity management for CAD modeling.

2.3 Overview of Multibody System Dynamics (MSD)

In modern mechanical engineering, multibody systems are a broad class of articulated mechanical systems that encompass mechanisms and machines [91]. More specifically, multibody systems are characterized by three fundamental features: 1) component bodies (rigid or flexible); 2) kinematic joints (ideal or real); 3) mechanical actions (internal or external). Thus, a multibody system can be thought of as a set of rigid or deformable mechanical components interconnected with each other by kinematic constraints and subjected to generalized force fields and/or applied forces. A schematic representation of the mechanical model of a typical multibody system is shown in Figure 2.

From a general perspective, Figure 2 schematically shows that a multibody system is a complex mechanical system composed of several elements. Specifically, this analysis includes rigid bodies, holonomic or nonholonomic kinematic constraints, nonlinear force fields or elements, and external actuators or control sensors. In the case of rigid multibody systems, the kinematics of a rigid body is entirely defined by that of a body-fixed reference system attached to each body. As a result, the local position of an arbitrary material point P belonging to the rigid body is described in terms of the location and orientation of the body-fixed frame of reference. The mathematical reference tool used for this purpose is known as the fundamental equation of rigid kinematics, which is defined as follows:

$$\boldsymbol{r}(P) = \boldsymbol{R} + \boldsymbol{u}(P) = \boldsymbol{R} + \boldsymbol{A}\bar{\boldsymbol{u}}(P) \tag{5}$$

where $d = 3$ is the space dimension, $\boldsymbol{r}(P)$ represents the global position vector having dimension $d \times 1$ of the material point P attached to the rigid body, $\boldsymbol{R}$ denotes the global position vector having dimension $d \times 1$ of the origin O of the body-fixed reference system, $\boldsymbol{u}(P)$ is the global position vector having dimension $d \times 1$ of the material point P, $\boldsymbol{A}$ is the rotation matrix having dimension $d \times d$ of the rigid body, and $\bar{\boldsymbol{u}}(P)$ is the local position vector having dimension $d \times 1$ of the material point P. It is worth noting that, from a mathematical perspective, Equation (5) can be interpreted as a field equation that relates the local position vector of the material point P to its global counterpart.

Additionally, the velocity and acceleration fields of the rigid body can be readily determined analytically by evaluating the first and second derivatives of the rigid body position field with respect to time as $\boldsymbol{v}(P) = \dot{\boldsymbol{r}}(P)$ and $\boldsymbol{a}(P) = \dot{\boldsymbol{v}}(P) = \ddot{\boldsymbol{r}}(P)$. In order to achieve this, one can write:

$$\boldsymbol{v}(P) = \dot{\boldsymbol{R}} + \boldsymbol{\omega} \times \boldsymbol{u}(P) = \dot{\boldsymbol{R}} + \boldsymbol{A}\left(\bar{\boldsymbol{\omega}} \times \bar{\boldsymbol{u}}(P)\right) \tag{6}$$

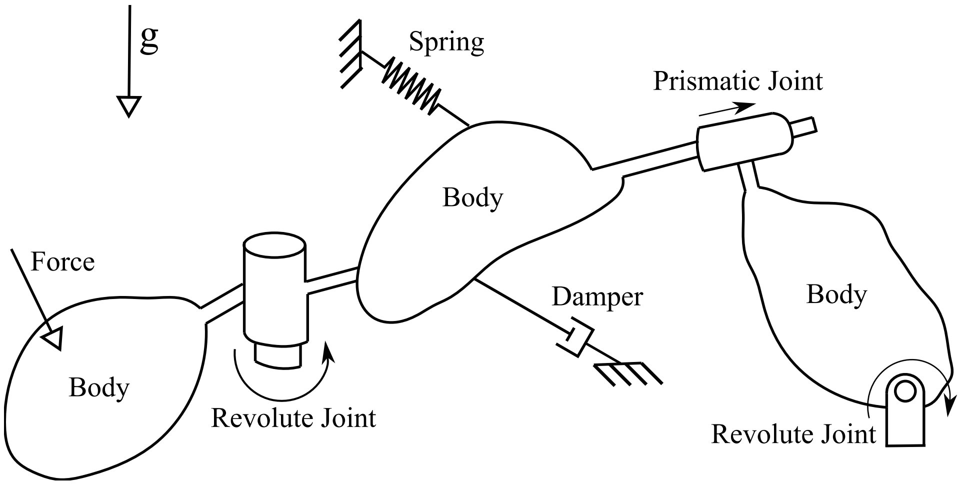

Fig. 2. Schematic representation of a multibody mechanical system model.

and

$$\boldsymbol{a}(P) = \ddot{\boldsymbol{R}} + \boldsymbol{\alpha} \times \boldsymbol{u}(P) + \boldsymbol{\omega} \times (\boldsymbol{\omega} \times \boldsymbol{u}(P)) = \ddot{\boldsymbol{R}} + \boldsymbol{A}\left(\bar{\boldsymbol{\alpha}} \times \bar{\boldsymbol{u}}(P)\right) + \boldsymbol{A}\left(\bar{\boldsymbol{\omega}} \times (\bar{\boldsymbol{\omega}} \times \bar{\boldsymbol{u}}(P))\right) \tag{7}$$

where $\boldsymbol{v}(P)$ and $\boldsymbol{a}(P)$ respectively represent the global velocity and acceleration vectors having dimension $d \times 1$ of the material point P attached to the rigid body, $\dot{\boldsymbol{R}}$ and $\ddot{\boldsymbol{R}}$ respectively denotes the global velocity and acceleration vectors having dimension $d \times 1$ of the origin O of the body-fixed reference system, $\boldsymbol{\omega}$ and $\bar{\boldsymbol{\omega}}$ respectively identify the global and local angular velocity vectors having dimension $d \times 1$ of the rigid body, whereas $\boldsymbol{\alpha}$ and $\bar{\boldsymbol{\alpha}}$ respectively define the global and local angular acceleration vectors having dimension $d \times 1$ of the rigid body. In analogy with Equation (5), Equations (6) and (7) can be interpreted as field equations that relate the local position vector of the material point P to its corresponding global velocity and acceleration vectors, respectively. Furthermore, although the second formulations in Equations (5), (6), and (7) are mathematically equivalent to the first formalism, it is more convenient to employ them in the kinematic description of complex multibody systems.

On the other hand, it can be readily demonstrated that the velocity and acceleration fields of a rigid body can be respectively expressed as linear functions of the generalized velocities and accelerations as follows:

$$\boldsymbol{v}(P) = \boldsymbol{L}(P)\dot{\boldsymbol{q}}, \quad \boldsymbol{a}(P) = \boldsymbol{L}(P)\ddot{\boldsymbol{q}} + \dot{\boldsymbol{L}}(P)\dot{\boldsymbol{q}} \tag{8}$$

being:

$$\boldsymbol{q} = \begin{bmatrix} \boldsymbol{R} \\ \boldsymbol{\theta} \end{bmatrix} \tag{9}$$

where p is the number of orientation parameters assumed in the kinematic description of the rigid body, $n_d = d$, $n_r = p$, and $n_b = n_d + n_r$ respectively denote the total number of displacement, rotational, and generalized coordinates of the rigid body, $\boldsymbol{q}$ is the body generalized coordinate vector having dimension $n_b \times 1$, $\boldsymbol{R}$ and $\boldsymbol{\theta}$ respectively define the displacement and rotational coordinate vectors of the rigid body having respectively dimensions $n_d \times 1$ and $n_r \times 1$, and $\boldsymbol{L}(P)$ represents the Jacobian matrix having dimension $d \times n_b$ of the rigid body position field.

The Jacobian matrix of the rigid body position field, represented by $\boldsymbol{L}(P)$, is a matrix that describes the linear transformation of the coordinates of a rigid body in the space of dimension d and is explicitly given by:

$$\boldsymbol{L}(P) = \begin{bmatrix} \boldsymbol{I} & \boldsymbol{A}\,\tilde{\bar{\boldsymbol{u}}}^T(P)\,\bar{\boldsymbol{G}} \end{bmatrix} \tag{10}$$

where $\boldsymbol{I}$ represents the identity matrix having dimension $d \times d$, $\tilde{\bar{\boldsymbol{u}}}(P)$ identifies the skew-symmetric matrix having dimension $d \times d$ associated with the cross product per the local position vector $\bar{\boldsymbol{u}}(P)$ of the material point P, and $\bar{\boldsymbol{G}}$ denotes the transformation matrix that enables the representation of the local angular velocity vector of the rigid body $\bar{\boldsymbol{\omega}}$ as a linear combination of the body rotational coordinates time derivatives $\dot{\boldsymbol{\theta}}$.

The equations of motion of a rigid multibody system can be systematically derived from the fundamental principles of analytical dynamics, yielding a nonlinear system of differential-algebraic equations composed of n_q differential equations and n_c algebraic equations, where n_q is the total number of system generalized coordinates and n_c is the total number of system algebraic constraints. By applying these principles in conjunction with the mathematical technique of analytical dynamics, which introduces Lagrange multipliers, the differential-algebraic equations of motion for the multibody system under study are obtained. By so doing, the differential-algebraic set of dynamic equations expressed in configuration space assumes the following so-called index-3 form:

$$\begin{cases} \boldsymbol{M}\ddot{\boldsymbol{q}} = \boldsymbol{Q}_v + \boldsymbol{Q}_e - \boldsymbol{C}_{\boldsymbol{q}}^T \boldsymbol{\lambda} \\ \boldsymbol{C} = \boldsymbol{0} \end{cases} \tag{11}$$

where $\boldsymbol{M}$ denotes the system mass matrix of dimensions $n_q \times n_q$, $\boldsymbol{Q}_v$ is the system quadratic velocity vector of dimensions $n_q \times 1$ capturing the centrifugal and Coriolis inertia terms, $\boldsymbol{Q}_e$ represents the generalized external force vector of dimensions $n_q \times 1$ associated with the conservative and nonconservative mechanical actions, and $\boldsymbol{C}_q = \partial \boldsymbol{C}/\partial \boldsymbol{q}$ identifies the constraint Jacobian matrix of dimensions $n_c \times n_q$ derived from the total constraint vector $\boldsymbol{C}$ of dimensions $n_c \times 1$, which encapsulates all kinematic joint constraints and is related to the additional vector of unknowns $\boldsymbol{\lambda}$ of dimensions $n_c \times 1$, which contains the Lagrange multipliers associated with these constraints.

As mentioned above, the system equations of motion given by Equation (11) represent a set of index-3 differential-algebraic equations. These equations can be transformed into their index-1 counterpart by replacing the position-level algebraic equations with their acceleration-level counterparts, obtained by taking the second time derivative of the mathematical equations that describe the kinematic constraints. By doing so, one obtains the following equivalent form of the dynamic model describing the multibody system under study:

$$\begin{cases} \boldsymbol{M}\ddot{\boldsymbol{q}} = \boldsymbol{Q}_v + \boldsymbol{Q}_e - \boldsymbol{C}_{\boldsymbol{q}}^T\boldsymbol{\lambda} \\ \boldsymbol{C}_{\boldsymbol{q}}\ddot{\boldsymbol{q}} = \boldsymbol{Q}_d \end{cases} \tag{12}$$

where $\boldsymbol{Q}_d$ represents the system quadratic velocity vector of dimensions $n_c \times 1$ containing the algebraic constraint analytical terms that are quadratic. Thus, Equation (12) represents a set of index-1 differential-algebraic equations of motion and encompasses all the kinematic constraints meaningful for performing the dynamic analysis.

In constrained multibody dynamics based on the index-1 form of the equations of motion, numerical time integration generally fails to preserve the algebraic constraint manifolds exactly, leading to minor time discretization errors that accumulate into constraint drift and progressively violate position-level and velocity-level constraints unless corrective measures are applied. In other words, standard time integrators do not preserve algebraic joint constraints exactly, so truncation errors accumulate, and the state drifts off the constraint manifold unless stabilization or projection is used. Therefore, two fundamental approaches are used to address this issue: the augmented formulation and the embedding technique.

The augmented formulation enforces constraints via Lagrange multipliers, yielding a sparse set of differential-algebraic equations that provide reaction forces and broad applicability. Still, it can enlarge the system, be ill-conditioned, and typically require drift control. On the other hand, the embedding technique absorbs local loop-closure constraints into an equivalent tree model, enabling recursive dynamics. Yet, it is mainly effective for local closures and may face rank changes or singular configurations. Furthermore, both approaches must be used in conjunction with a constraint stabilization method, such as the robust generalized coordinate partitioning method or the direct correction method [92].

Adopting the augmented formulation, the nonlinear differential-algebraic equations of motion can be arranged in the following compact form:

$$\begin{bmatrix} \boldsymbol{M} & \boldsymbol{C}_{\boldsymbol{q}}^T \\ \boldsymbol{C}_{\boldsymbol{q}} & \boldsymbol{O} \end{bmatrix} \begin{bmatrix} \ddot{\boldsymbol{q}} \\ \boldsymbol{\lambda} \end{bmatrix} = \begin{bmatrix} \boldsymbol{Q}_v + \boldsymbol{Q}_e \\ \boldsymbol{Q}_d \end{bmatrix} \tag{13}$$

Solving the linear system of algebraic equations encapsulated in Equation (13) provides both the generalized acceleration vector $\ddot{\boldsymbol{q}}$ and the Lagrange multiplier vector $\boldsymbol{\lambda}$. The Lagrange multipliers are essential for determining the generalized constraint force vector, while the system generalized accelerations facilitate the use of standard numerical integration to advance the simulation in time. By so doing, dynamical simulations based on the equations of motion of a multibody system can be readily carried out, thereby exploring several engineering scenarios of practical interest.

2.4 Overview of Finite Element Analysis (FEA)

The Finite Element Method (FEM) is a computational approach that divides the geometry of a mechanical system into discrete regions, or elements, to facilitate the numerical solution of complex mechanical problems that are typical of structural engineering. Over the years, several types of two-dimensional and three-dimensional finite elements have been developed within the field of finite element technology [93]. Thus, the Finite Element Method (FEM) represents a comprehensive computational tool for structural analysis of mechanical components with complex geometric shapes and realistic material properties.

In this study, a quadratic tetrahedral element, shown in Figure 3, is employed in the finite element discretization, whose geometry is defined by nodes at its vertices and midpoints along its edges, thereby enabling the capture of positions and displacement gradients at the finite element nodes with enhanced precision.

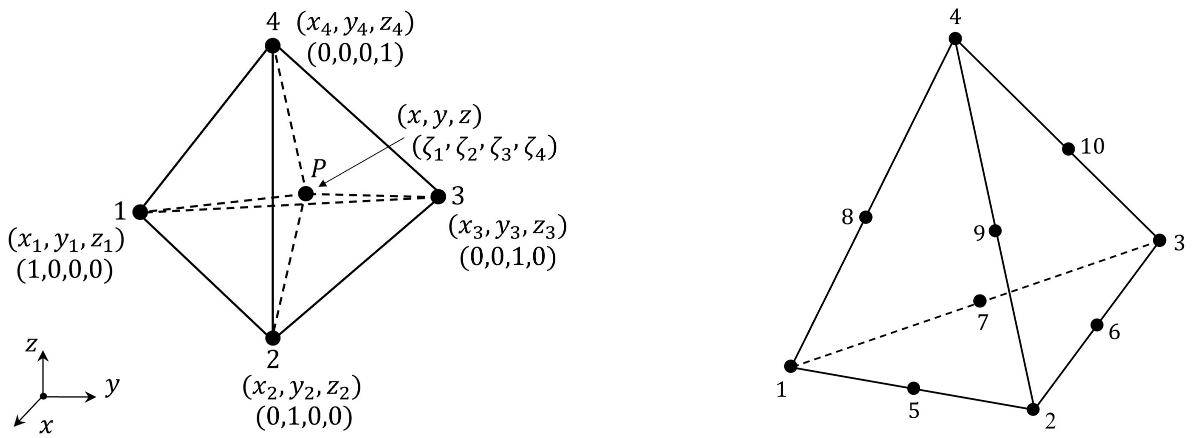

(a) Dimensionless volume coordinates.

(b) Finite element nodes.

Fig. 3. Dimensionless volume coordinates and location of nodes in a quadratic tetrahedron finite element. (a) Quadratic tetrahedron dimensionless volume coordinates. (b) Quadratic tetrahedron finite element nodes.

As illustrated in Figure 3a, the four natural or tetrahedral coordinates of the quadratic tetrahedral element are respectively denoted with ζ_1, ζ_2, ζ_3, and ζ_4. In the case of a quadratic interpolation, there are 10 nodal unknowns, one at each of the nodes indicated in Figure 3b. More specifically, observing Figure 3, the nodes 1, 2, 3, and 4 correspond to the corner nodes, whereas the nodes 5, 6, 7, 8, 9, and 10 are located at the midpoints of the edges of the tetrahedron.

The dimensionless volume coordinates of the quadratic tetrahedron finite element shown in Figure 3 are defined as:

$$\zeta_1 = \frac{V_1}{V},\ \zeta_2 = \frac{V_2}{V},\ \zeta_3 = \frac{V_3}{V},\ \zeta_4 = \frac{V_4}{V} \tag{14}$$

where $V_i,\ i = 1, 2, 3, 4$ is the volume of the tetrahedron associated with the material point P and the vertices other than the vertex i, and V is the total volume of the tetrahedron element defined by the vertices 1, 2, 3, and 4. The aforementioned volume coordinates can be mathematically expressed as:

$$\begin{bmatrix} 1 \\ x \\ y \\ z \end{bmatrix} = \begin{bmatrix} 1 & 1 & 1 & 1 \\ x_1 & x_2 & x_3 & x_4 \\ y_1 & y_2 & y_3 & y_4 \\ z_1 & z_2 & z_3 & z_4 \end{bmatrix} \begin{bmatrix} \zeta_1 \\ \zeta_2 \\ \zeta_3 \\ \zeta_4 \end{bmatrix} \tag{15}$$

which leads to:

$$\begin{bmatrix} \zeta_1 \\ \zeta_2 \\ \zeta_3 \\ \zeta_4 \end{bmatrix} = \frac{1}{6V} \begin{bmatrix} 6V_1 & L_{1,1} & L_{1,2} & L_{1,3} \\ 6V_2 & L_{2,1} & L_{2,2} & L_{2,3} \\ 6V_3 & L_{3,1} & L_{3,2} & L_{3,3} \\ 6V_4 & L_{4,1} & L_{4,2} & L_{4,3} \end{bmatrix} \begin{bmatrix} 1 \\ x \\ y \\ z \end{bmatrix} \tag{16}$$

where:

$$\begin{bmatrix} 1 & 1 & 1 & 1 \\ x_1 & x_2 & x_3 & x_4 \\ y_1 & y_2 & y_3 & y_4 \\ z_1 & z_2 & z_3 & z_4 \end{bmatrix}^{-1} = \frac{1}{6V} \begin{bmatrix} 6V_1 & L_{1,1} & L_{1,2} & L_{1,3} \\ 6V_2 & L_{2,1} & L_{2,2} & L_{2,3} \\ 6V_3 & L_{3,1} & L_{3,2} & L_{3,3} \\ 6V_4 & L_{4,1} & L_{4,2} & L_{4,3} \end{bmatrix} \tag{17}$$

being $x_i,\ y_i,\ z_i,\ i = 1, 2, 3, 4$ the Cartesian coordinates of the tetrahedron corner nodes $1, 2, 3$, and 4 [94].

In general, by using the principle of separation of variables, the displacement field of a given tetrahedral finite element can be written in terms of the nodal coordinates, as well as by using the set of shape functions, as follows:

$$\boldsymbol{r}(P) = \boldsymbol{N}(P)\boldsymbol{e} \tag{18}$$

being:

$$\boldsymbol{N}(P) = \begin{bmatrix} N_1(P)\boldsymbol{I} & N_2(P)\boldsymbol{I} & \dots & N_{10}(P)\boldsymbol{I} \end{bmatrix} \tag{19}$$

where $d = 3$ is the space dimension, $n_k = 10$ is the number of nodes equal to the number of shape functions associated with the quadratic tetrahedron, $n_e = dn_k = 30$ denotes the total number of nodal coordinates associated with the nodal displacements, $\boldsymbol{r}(P)$ is a $d \times 1$ vector describing the global position vector of an arbitrary material point P belonging to the volume of the tetrahedral finite element, $\boldsymbol{N}(P)$ is a $d \times n_e$ matrix containing the element shape functions $N_k(P),\ k = 1, 2, \dots, n_k$ depending on the material point P, $\boldsymbol{I}$ stands for the identity matrix of dimensions $d \times d$, and $\boldsymbol{e}$ is a $n_e \times 1$ vector containing the finite element nodal coordinates. The analytical form of the quadratic tetrahedron shape functions $N_k(P),\ k = 1, 2, \dots, n_k$ is provided below:

$$\begin{cases} N_1(P) = \zeta_1(2\zeta_1 - 1),\ N_2(P) = \zeta_2(2\zeta_2 - 1) \\ N_3(P) = \zeta_3(2\zeta_3 - 1),\ N_4(P) = \zeta_4(2\zeta_4 - 1) \end{cases} \tag{20}$$

and

$$\begin{cases} N_5(P) = 4\zeta_1\zeta_2,\ N_6(P) = 4\zeta_2\zeta_3 \\ N_7(P) = 4\zeta_1\zeta_3,\ N_8(P) = 4\zeta_1\zeta_4 \\ N_9(P) = 4\zeta_2\zeta_4,\ N_{10}(P) = 4\zeta_3\zeta_4 \end{cases} \tag{21}$$

Furthermore, in the case of the quadratic tetrahedral finite element employed in this work, the nodal coordinate vector denoted with **e** can be written as:

$$\boldsymbol{e} = \begin{bmatrix} \boldsymbol{r}_1^T & \boldsymbol{r}_2^T & \dots & \boldsymbol{r}_{10}^T \end{bmatrix} \tag{22}$$

where $\boldsymbol{r}_k,\ k = 1, 2, \dots, n_k$ are the global position vectors of the generic nodal points labeled with the integer k of the quadratic tetrahedral finite element shown in Figure 3.

Consider now a finite element mesh made of N_e finite elements, in which the integer j identifies the specific element referred to in the present analysis. In the context of static structural analysis, the primary objective is to determine the equilibrium configuration of the mechanical system under specified external loads and boundary conditions. In the absence of significant inertial effects, the equilibrium equation can be written as follows:

$$\boldsymbol{Q}_b = \boldsymbol{Q}_s + \boldsymbol{Q}_e = \boldsymbol{0} \tag{23}$$

where n_q is the total number of generalized coordinates of the finite element mesh, $\boldsymbol{Q}_b$ represents the total vector of generalized external forces of dimensions $n_q \times 1$, $\boldsymbol{Q}_s$ is the vector of generalized elastic forces having dimensions $n_q \times 1$ derived from the element elastic deformation, and $\boldsymbol{Q}_e$ is the vector of applied external forces of dimensions $n_q \times 1$. Assuming a linear elastic problem, the generalized elastic force vector $\boldsymbol{Q}_s$ of the finite element mesh can be approximated, retaining only its linear mathematical part, as follows:

$$\boldsymbol{Q}_s \simeq -\boldsymbol{K}\boldsymbol{q} \tag{24}$$

where $\boldsymbol{q}$ is an $n_q \times 1$ vector containing all the nodal displacements of the finite element mesh, representing the total set of generalized coordinates, and $\boldsymbol{K}$ is the stiffness matrix of the finite element mesh having dimensions $n_q \times n_q$. When the approximation of Equation (24) is combined with the equilibrium conditions given in Equation (23), one obtains:

$$\boldsymbol{K}\boldsymbol{q} = \boldsymbol{Q}_e \tag{25}$$

As mentioned before, $\boldsymbol{K}$ is the $n_q \times n_q$ stiffness matrix of the finite element model, constructed by assembling the stiffness matrices of individual elements and incorporating the boundary conditions, and $\boldsymbol{q}$ represents the total vector of nodal coordinates. For each tetrahedral finite element j that forms the final structural mesh of N_e elements, the element stiffness matrix $\boldsymbol{K}_j$ having dimensions $n_e \times n_e$ is computed as follows:

$$\boldsymbol{K}_j = \int_{V_{b,j}} \boldsymbol{L}_{v,j}^T \boldsymbol{E}_j \boldsymbol{L}_{v,j} dV_j, \quad j = 1, 2, \dots, N_e \tag{26}$$

where $V_{b,j}$ is the total volume of the continuous body j, $\boldsymbol{E}_j$ represents the matrix of elastic coefficients of dimensions $2d \times 2d$ defined in accordance with the Voigt notation for the material stress-strain relationship of element j, and $\boldsymbol{L}_{v,j}$ denotes a matrix of position vector gradients having dimensions $2d \times n_e$, which are derived from the shape functions of the quadratic tetrahedral finite element.

Under the assumption of linear elastic behavior and in the presence of small deformations, the material properties of each element j are defined by the modulus of elasticity E_j and Poisson ratio ν_j. Thus, the elasticity matrix $\boldsymbol{E}_j$ is given by:

$$\boldsymbol{E}_j = C_j \begin{bmatrix} \boldsymbol{A}_j & \boldsymbol{O} \\ \boldsymbol{O} & \boldsymbol{B}_j \end{bmatrix}, \quad j = 1, 2, \ldots, N_e \tag{27}$$

being:

$$\boldsymbol{A}_j = \begin{bmatrix} 1-\nu_j & \nu_j & \nu_j \\ \nu_j & 1-\nu_j & \nu_j \\ \nu_j & \nu_j & 1-\nu_j \end{bmatrix}, \quad j = 1, 2, \ldots, N_e \tag{28}$$

and

$$\boldsymbol{B}_j = \begin{bmatrix} \frac{1-2\nu_j}{2} & 0 & 0 \\ 0 & \frac{1-2\nu_j}{2} & 0 \\ 0 & 0 & \frac{1-2\nu_j}{2} \end{bmatrix}, \quad j = 1, 2, \ldots, N_e \tag{29}$$

where $\boldsymbol{O}$ is a null matrix of dimensions $d \times d$ and C_j is an elasticity constant of the finite element j defined as follows:

$$C_j = \frac{E_j}{(1+\nu_j)(1-2\nu_j)}, \quad j = 1, 2, \ldots, N_e \tag{30}$$

Additionally, the gradient matrix $\boldsymbol{L}_{v,j}$ associated with the finite element j is mathematically formulated as:

$$\boldsymbol{L}_{v,j} = \begin{bmatrix} \boldsymbol{r}_{x,j}^T \boldsymbol{N}_{x,j} \\ \boldsymbol{r}_{y,j}^T \boldsymbol{N}_{y,j} \\ \boldsymbol{r}_{z,j}^T \boldsymbol{N}_{z,j} \\ \boldsymbol{r}_{x,j}^T \boldsymbol{N}_{y,j} + \boldsymbol{r}_{y,j}^T \boldsymbol{N}_{x,j} \\ \boldsymbol{r}_{x,j}^T \boldsymbol{N}_{z,j} + \boldsymbol{r}_{z,j}^T \boldsymbol{N}_{x,j} \\ \boldsymbol{r}_{y,j}^T \boldsymbol{N}_{z,j} + \boldsymbol{r}_{z,j}^T \boldsymbol{N}_{y,j} \end{bmatrix}, \quad j = 1, 2, \ldots, N_e \tag{31}$$

where $\boldsymbol{r}_{x,j} = \partial \boldsymbol{r}_j / \partial x$, $\boldsymbol{r}_{y,j} = \partial \boldsymbol{r}_j / \partial y$, and $\boldsymbol{r}_{z,j} = \partial \boldsymbol{r}_j / \partial z$ represent the components of the global position vector gradients in the direction of each spatial coordinate of the element j, while $\boldsymbol{N}_{x,j} = \partial \boldsymbol{N}_j / \partial x$, $\boldsymbol{N}_{y,j} = \partial \boldsymbol{N}_j / \partial y$, and $\boldsymbol{N}_{z,j} = \partial \boldsymbol{N}_j / \partial z$ are the partial derivatives of the shape function matrix of the element j in the corresponding directions.

The final equilibrium configuration is obtained by solving the resulting system of linear algebraic equations. Thus, the finite element analysis methodology is applicable to a range of element types. However, in this study, the quadratic tetrahedral element is employed to achieve greater precision in structural response modeling.

2.5 Proposed Approach for Integration of Computer-Aided Design and Analysis (I-CAD-A)

The Integration of Computer-Aided Design and Analysis (I-CAD-A) refers to the smooth combination of CAD (design) and CAE (analysis, synthesis, and simulation) tools. It allows engineers to create, evaluate, and enhance products within a single cohesive platform. Computational methods such as the Absolute Nodal Coordinate Formulation (ANCF) and Isogeometric Analysis (IGA) often link geometric models directly to analysis meshes. The goal of this integration is to facilitate a seamless workflow from initial design and virtual testing to manufacturing. Therefore, this integration will eventually eliminate data translation issues, improve accuracy, and accelerate product development by providing real-time performance feedback on designs. The main features of the computational approaches aimed at achieving the I-CAD-A are discussed below.

In the literature, one proposed solution to the I-CAD-A is a mechanics-based unification strategy that eliminates the conventional CAD-to-analysis translation paradigm by adopting the ANCF approach as a common geometric-computational representation. This approach directly addresses the root cause of I-CAD-A failure, which is not merely file-format incompatibility. Instead, the deeper inconsistency lies between tolerance-driven CAD models and trimmed NURBS boundary representations, constructed to preserve design intent, and the requirements of multibody dynamics and finite element analysis, which demand numerically robust, topologically consistent, and discretization-ready domains. This approach exploits the isoparametric property of ANCF finite elements, in which the same interpolation functions define both geometry and deformation, allowing ANCF elements for beams, plates, and shells to serve simultaneously as curve/surface generators and as analysis-ready continuum discretizations.

By adopting a consistent geometric representation, such as the ANCF, the fragile, error-prone sequence of geometry healing, meshing, and model reduction is replaced with a single-source description in which kinematics, inertia, and elasticity are embedded directly in the geometric representation. In this framework, flexible multibody dynamics, contact, and constraints are formulated consistently in the same nodal coordinate space used to define geometry, enabling high geometric fidelity without sacrificing the numerical conditioning required for MSD and FEA. Consequently, this solution for the I-CAD-A is not a translator but a reformulation, namely a unified computational geometry that inherently supports both finite element discretization and multibody system dynamics within a single mathematically coherent model.

The computational formulation mentioned above for the I-CAD-A is very effective and will eventually lead to modern mechanical engineering tools. However, this approach is extremely radical and does not allow for exploiting existing high-performance CAE tools to integrate CAD-MBD-FEA engineering analysis. On the other hand, another possible approach for achieving the I-CAD-A is to adopt a sequential computational framework based on the linear theory of elastodynamics. The linear theory of elastodynamics is formulated as a practical partitioned approach for incorporating structural flexibility into multibody system simulations while preserving the computational efficiency of classical rigid-body dynamics. The central assumption is that the rigid-body motion of each component, including the evolution of body-fixed reference frames and orientations, is first determined using standard multibody equations of motion, with kinematic constraints enforced at the system level. The elastic deformation field is not solved concurrently with the rigid motion. Instead, it is reconstructed in a postprocessing stage by treating each flexible component as a linear elastic continuum subjected to the previously computed rigid-body kinematics. In this setting, deformation is assumed small relative to the overall motion, thereby justifying the use of linear elastodynamic field equations and structural dynamic discretizations based on finite elements or truncated modal expansions with constant mass and stiffness operators.

It is important to note that the sequential decoupling approach based on linear elastodynamics yields a substantial reduction in computational complexity, mitigates numerical stiffness, and enables the direct reuse of well-established rigid-body integration algorithms and constraint enforcement procedures. The approach is, nevertheless, constrained by its underlying linearization and the absence of strong two-way coupling during time integration. Consequently, its predictive accuracy diminishes when geometric nonlinearities, large elastic strains, or pronounced inertial-elastic interactions become significant. Under such conditions, as discussed above, fully coupled nonlinear elastodynamic formulations are required to capture the interaction between rigid-body motion and structural deformation.

To summarize, this investigation adopts a sequential approach grounded in the linear theory of elastodynamics, resulting in an integrated methodology that combines CAD, MBD, and FEM simulations, as schematized in Figure 4. This iterative process represents a practical approach that can be applied to analyze mechanical systems, where reliability and durability are fundamental, as discussed in detail below.

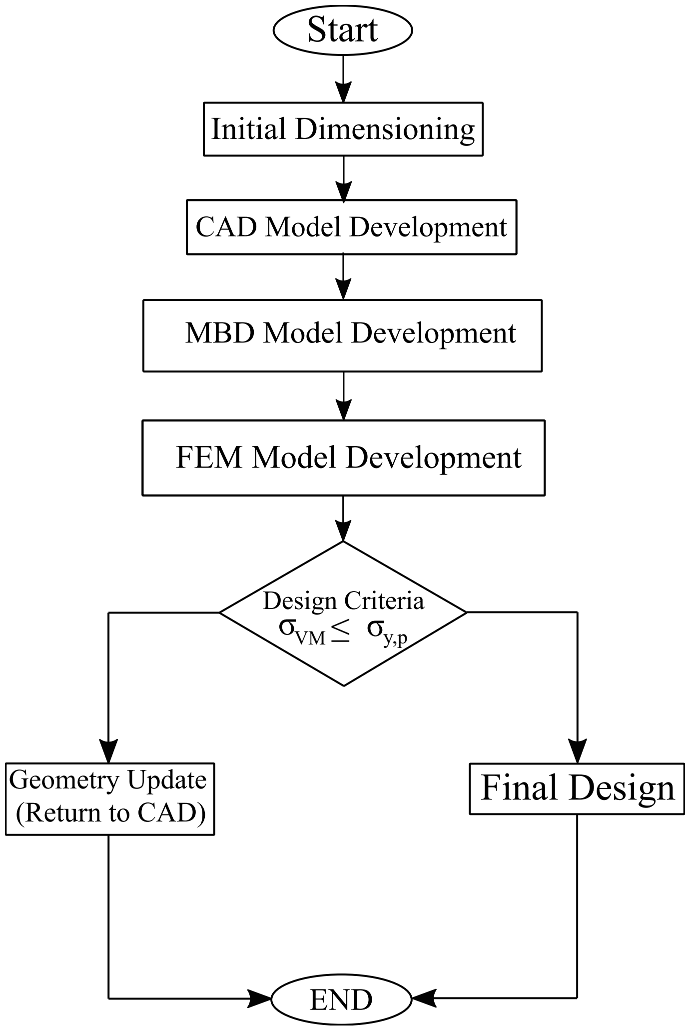

Fig. 4. Schematic flowchart representing the integrated CAD-MBD-FEM methodology adopted in this investigation.

The schematic representation of this methodology, as outlined in Figure 4, provides a visual illustration of its fundamental steps and their interrelationships. This approach enabled the assessment of both the forces acting on the system and the structural response of individual components, thereby establishing an integrated CAD-MBD-FEM framework for the virtual prototyping of a new deployment mechanism for a foldable propulsor support in urban air mobility vehicles, which serves as the main case study of this research work.

As mentioned above, one of the significant contributions of this research is the iterative design process schematized in Figure 4, which permitted gradual enhancements in the geometry of the pins and the arm. By incrementally increasing the pin diameter and the arm section thickness, the final design satisfied the required safety standards while maintaining structural efficiency. As mentioned earlier, the approach based on the FEM is particularly effective for identifying regions susceptible to failure due to elevated stress concentrations.

In the context of flying cars, components such as pins and arms of the deployable mechanism are subjected to considerable bending and shear forces. By employing FEM, engineers can forecast the locations where these forces will exert the most significant strain and subsequently modify the component geometry or material properties to optimize its performance. For instance, increasing the thickness of specific regions or modifying material properties may reduce the probability of failure while maintaining the mechanism overall weight within acceptable limits. Thus, the concept design and preliminary sizing of the main case study are provided in the paper below, followed by the numerical results obtained using the integrated CAD-MBD-FEM approach proposed in this investigation.

3. Concept Design and Preliminary Sizing

3.1 System Concept Definition and Estimation of Acting Forces

Flying car prototypes represent one of the latest developments in the field of advanced mobility. These prototypes combine innovative solutions in structural design, modularity, and aerodynamic optimization, as shown in [95]. The use of advanced rigid and flexible numerical models enables more accurate analysis of system dynamics, providing critical information for safety assessment and system-wide optimization [96]. Consistent with this trend, the literature shows a growing interest in eVTOL vehicles and configurations similar to flying cars. In addition to design and optimization using advanced simulation techniques, monitoring and control play an important role [97]. In this context, Digital Twins (DTs) serves as a particularly effective tool for real-time monitoring of the system. This tool enables the integration of real-world data with virtual models to assess the structural condition of the aircraft or optimize energy consumption [98].

From a design perspective, the aim is to develop a vehicle suitable for both air and ground transport. Therefore, the first step is to define the functional requirements of the current design idea, establish a preliminary vehicle concept, and understand the design domain in which it will operate in a realistic scenario to facilitate the transition toward the Urban Air Mobility (UAM) [99]. The preliminary concept design of the flying car with an opening mechanism for the engine and propeller supports, considered as the case study of this paper, is shown in Figure 5.

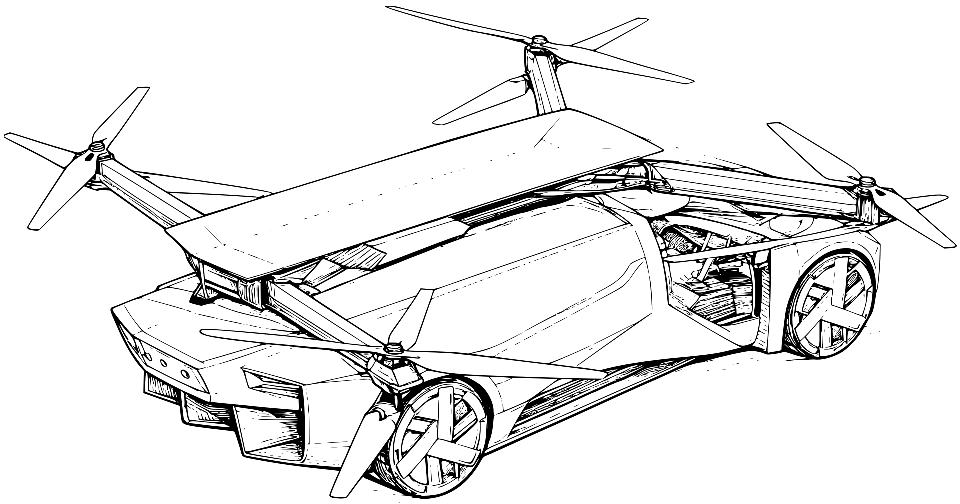

Fig. 5. Concept design of a flying car with an opening mechanism for the propulsor support.

In line with these developments, Figure 5 shows a graphic mockup inspired by the XPENG flying car [100], which is adopted as a conceptual model to illustrate the concept of flying cars. In this vein, the main problem is that a flying car cannot be simply treated as a large drone with wheels. It is a hybrid vehicle that must meet the constraints and requirements of both the aeronautical and automotive worlds. From an aeronautical perspective, the vehicle must be capable of vertical takeoff and landing, and must maintain stability during hovering maneuvers. From a ground-transport perspective, it must have a suitable footprint and an appropriate center of gravity. These considerations imply the need to develop a compact vehicle in which the elements for aerial locomotion can be automatically hidden or stowed when not in use. Therefore, attention shifts to creating a deployable motor support mechanism that can be opened when needed and closed during road transport.

The vehicle under investigation is thus equipped with an unconventional system, namely a deployable support mechanism. Given its function, this component is the most fundamental structural element of the architecture and therefore requires an advanced, unconventional, and targeted design. To properly approach its design, the first step is to determine the forces required to ensure the equilibrium of the car during flight. More importantly, the first fundamental step is to determine the necessary forces acting on this system to ensure the equilibrium of the entire vehicle in flight. For the sake of simplicity, a simplified aerial vehicle is considered here, as illustrated in Figure 6.

For simplicity, the mechanical system shown in Figure 6, capable of motion in two-dimensional Euclidean space, consists of a beam representing one-half of the aerial vehicle, sectioned along its longitudinal axis, and carrying motors at both ends. In this simplified preliminary model, the beam is assumed to rotate about its center of gravity by a pitch angle θ. To illustrate the preliminary sizing procedure, the design described herein assumes that the distances from the center of mass of the two motors are $L_1 = 1770$ (mm) and $L_2 = 794$ (mm), as shown in Figure 6. As the propellers rotate, two thrust forces, F_F and F_R, are exerted on the system. The external force F_F corresponds to the thrust force applied to the front arm, while the external force F_R refers to the thrust force applied to the rear arm.

Considering the force components in the x and z directions of the global reference system attached to the ground, as shown in Figure 6, the equilibrium conditions of the front and rear propellers about the global y axis must be satisfied. For this purpose, one can directly write:

$$\begin{cases} F_{F_Z} + F_{R_Z} = F_g \\ F_F L_1 = F_R L_2 \end{cases} \tag{32}$$

where $F_{F_Z} = F_F \cos(\theta)$ and $F_{R_Z} = F_R \cos(\theta)$ are the projections of the front propulsive force F_F and the rear propulsive force F_R onto the global z axis. Additionally, it is assumed that the maximum mass the vehicle can lift is $m_{max} = 450$ (kg), including two passengers, and that a safety factor F_s of 1.5 (-) should be applied [101]. This allows the maximum takeoff weight W_{max} to be obtained as follows:

$$W_{max} = F_s m_{max} g = 1.5\ (-) \cdot 450\ (\text{kg}) \cdot 9.81\ (\text{m/s}^2) = 6622\ (\text{N}) \tag{33}$$

Given that the complete vehicle is equipped with four arms, the force F_g exerted by each arm can be calculated as follows:

$$F_g = \frac{W_{max}}{2} = \frac{6622\ (\text{N})}{2} = 3311\ (\text{N}) \tag{34}$$

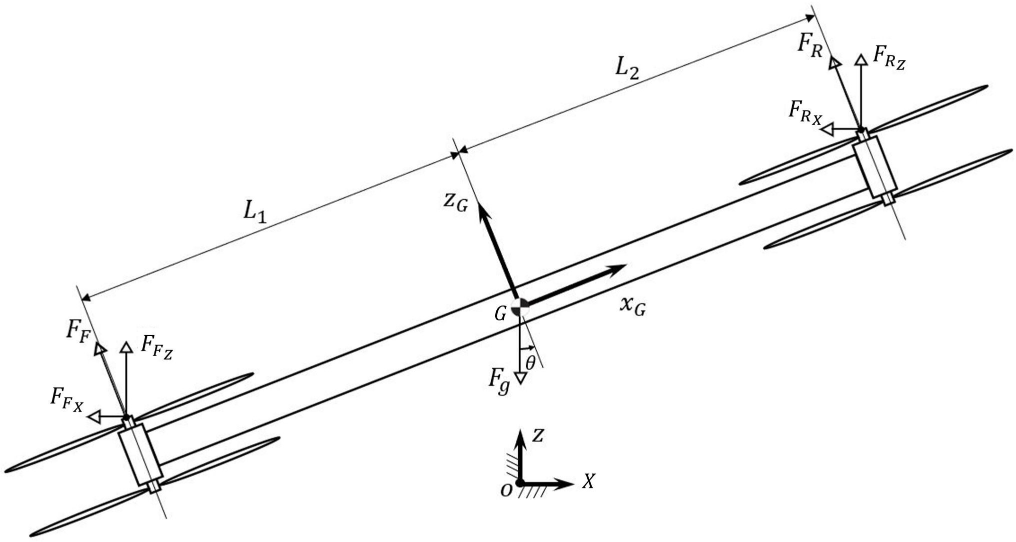

Fig. 6. Simplified mechanical model of the flying car concept with its opening mechanism for the propulsor support.

By using the relationships in Equation (32), one can readily calculate the thrust forces F_F and F_R acting on the front and rear sections of the aerial vehicle for a range of values of the pitch angle θ. To this end, by solving the set of algebraic equations representing the system equilibrium reported in Equation (32), one can write:

$$\begin{cases} F_F = \frac{F_g}{(1+\mu)\cos(\theta)} \\ F_R = \mu F_F \end{cases} \tag{35}$$

where $\mu = L_1/L_2 = 2.2292$ $(-)$. The data for the lift forces at varying values of the angle θ are presented in Table 1.

Table 1. Numerical values representing the magnitudes of the front thrust force F_F and the rear thrust force F_R for different values of the pitch angle θ.

θ (deg)	F_F (N)	F_R (N)
0	1025	2285
5	1029	2294
10	1041	2321
15	1062	2366
20	1091	2432
25	1131	2522
30	1183	2639
35	1252	2790
40	1339	2983
45	1450	3232

Based on the numerical data reported in Table 1, it is possible to carry out the initial dimensioning of the preliminary concept of flying car analyzed here, as discussed in detail below.

3.2 Initial Dimensioning

Before proceeding with the static analysis, the main kinematic characteristics of the mechanism are defined during this preliminary design phase. In particular, the opening and closing mechanism for the engine and propeller support is inspired by an articulated quadrilateral actuated by an electric cylinder. Accordingly, a schematic representation of the system is shown in Figures 7 and 8.

As shown in Figures 7 and 8, the deployable mechanism in this study is kinematically equivalent to a four-bar linkage, with element AD representing the actuator, element DE representing the crank, element EF representing the connecting rod, and element CP representing the arm.

As mentioned before, the preliminary design of the deployable mechanism analyzed here is shown in the closed configuration in Figure 7, while the open configuration is shown in Figure 8. Furthermore, Table 2 presents the dimensions of the mechanism elements, schematized in their open configuration, as shown in Figure 8.

In the preceding simplified structural analysis, the forces acting on the arm were determined. It is evident that the most critical scenario shown in Table 1 is flight at an angle of 45 degrees, specifically on the rear arm, where a force of 3232.1 (N) is required. This force will serve as a reference point for the subsequent pre-dimensioning process.

The most critical components are those that connect the various parts of the mechanism. Consequently, these components will be the focus of the subsequent structural analysis based on the preliminary mechanical model presented herein. By applying a force in the global z direction at point P in Figure 8, the reactions at the joints can be obtained. These values, calculated in the body reference frame x_i, y_i, z_i and illustrated in Table 3, will be used for the pre-dimensioning of the pins that join all the fundamental elements of the mechanism. In particular, the computational evaluation of the reaction forces of interest is performed using SIMSCAPE MULTIBODY software. Thus, a simplified schematic model of the propeller folding mechanism is constructed for

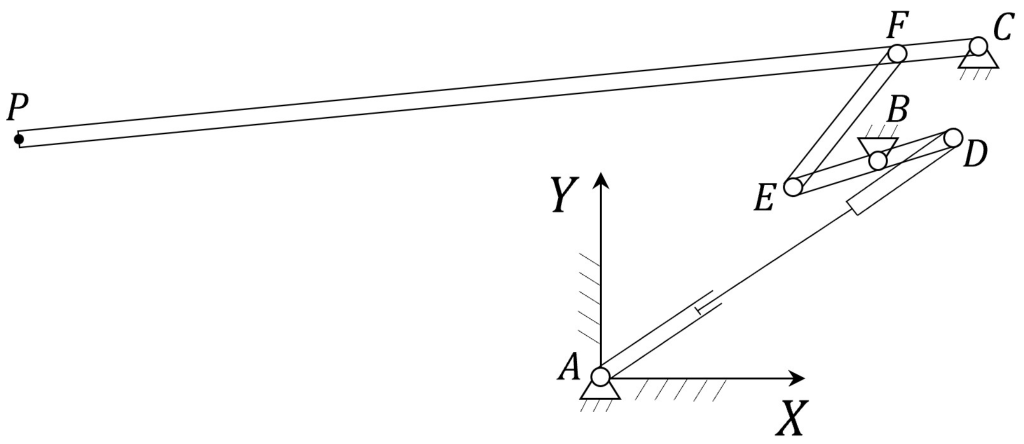

Fig. 7. Propeller folding mechanism schematization in the closed configuration.

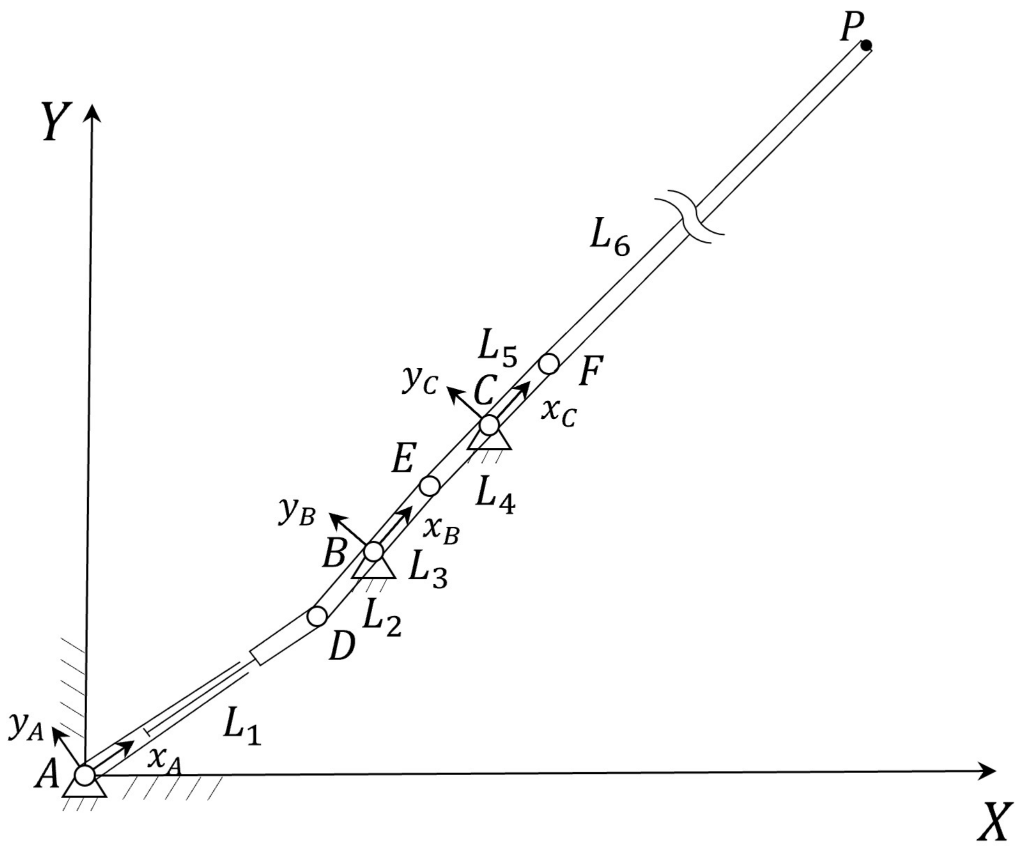

Fig. 8. Propeller folding mechanism schematization in the open configuration.

Table 2. Dimensions of the propeller folding mechanism elements in the open configuration.

Item	Segment	Length	Value (Units)
Actuator	$\overline{AD}$	L_1	311 (mm)
Crank	$\overline{DB}$	L_2	99 (mm)
	$\overline{BE}$	L_3	99 (mm)
Connecting rod	$\overline{EF}$	L_4	198 (mm)
Arm	$\overline{CF}$	L_5	20 (mm)
	$\overline{CP}$	L_6	1100 (mm)

its dynamic analysis, and a subsequent static analysis is conducted. For this purpose, the mechanism is fixed in the fully open configuration, and the maximum thrust force is applied at point P.

Overall, the opening mechanism is statically analyzed by developing a simplified multibody kinematic model of the mechanism shown in Figure 8, yielding numerical values for the reaction forces and moments at all mechanical joints, as shown in Table 3. Furthermore, the arm, which is directly actuated by the motors, will also undergo pre-dimensioning. Following this preliminary structural analysis, the pre-dimensioning of the pins and the arm is described in detail below.

Table 3. Numerical values of the reaction forces and moments of all the mechanical joints.

Component	Reaction	x axis	y axis	z axis
Pin A	Force (N)	0	0	209.1
	Moment (N×m)	288.7	-304.4	0
Pin B	Force (N)	0	0	-623.9
	Moment (N×m)	9.6	774.8	0
Pin C	Force (N)	0	0	-2399
	Moment (N×m)	8.4	2607	0

3.2.1 Pre-dimensioning of the Pins

It is inherent to the design of pins that they are not intended to withstand significant moments [102]. The primary function of pins is to resist axial forces and shear loads. However, they are not designed to withstand bending moments, as this can lead to premature failure [102]. To perform the pre-dimensioning of the pins, a bar of length $L_p = 80$ (mm) and a constant circular section S_p, initially unknown, is considered. This element is modeled as a simply supported beam, as illustrated in Figure 9. At its midpoint, the loads obtained in the preceding section are applied.

When moments are applied to pins, particularly in structural analysis, it is essential to convert them into equivalent shear forces. This is crucial to ensure a realistic and precise analysis of their mechanical behavior [30]. In calculating the equivalent stress using the Von Mises criterion, moments are replaced with equivalent shear forces, as illustrated in Figure 9. This approach provides a more physically representative approximation of the actual load distribution. It also avoids overestimating stresses in the pins, providing a more reliable assessment of their performance under the specified loading conditions.

Figure 9 shows a schematic representation of the forces acting on the pins. In particular, it shows a transformation of the loads into an equivalent set of forces, thereby converting the loading scenario in Figure 9a into that in Figure 9b. This transformation is necessary because the actual mechanical connection is not a simple hinge but a fork joint. As a result, the bending moment acting on the pin must be converted into an equivalent shear load to represent the stresses transmitted through the pivot.

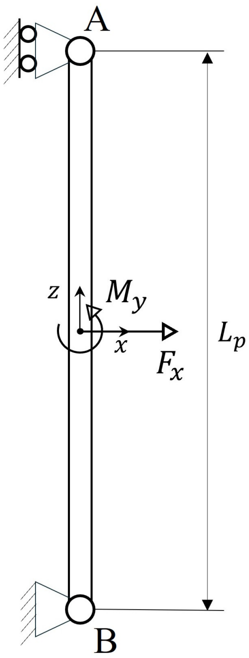

(a) Initial loads scheme.

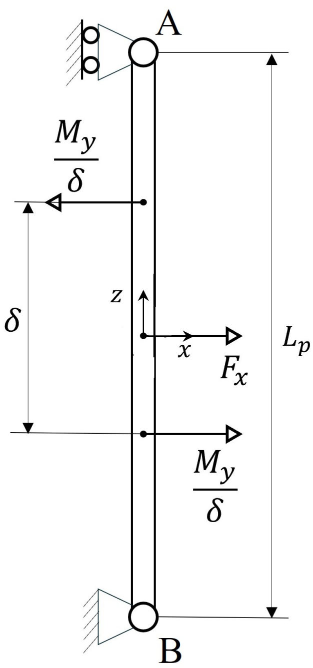

(b) Shear loads scheme.

Fig. 9. Schematization of the forces acting on the pin. (a) Two-dimensional representation of the pin subjected to the initial load configuration. (b) Equivalent two-dimensional representation with bending moments transformed into shear loads.

The bending moment and shear diagrams for the pin structural scheme shown in Figure 9b are illustrated in Figure 10, and the corresponding stress values are presented in Table 4. In Figure 10 and Table 4, T_i and M_i represent the shear force and the bending moment, respectively, associated with segment i of the pin, which is schematized as a beam element.

The bending moment and shear force diagrams are shown in Figure 9. These diagrams facilitate the analysis of critical points along the pin. The value of δ shown in Figure 9 and Table 4 is derived from a geometric relationship and takes the values 18 (mm), 42 (mm), and 54 (mm) for the pins A, B, and C in Figures 7 and 8, respectively.

In this type of elementary static analysis, the Von Mises stress σ_{VM} is typically employed, which can be calculated as follows [103]:

$$\sigma_{VM} = \sqrt{\sigma^2 + 3\tau^2} \tag{36}$$

where σ is the normal stress and τ is the shear stress, which can be readily computed by adopting the Euler-Bernoulli beam theory and the Jourawski approximate solution for shear stress.

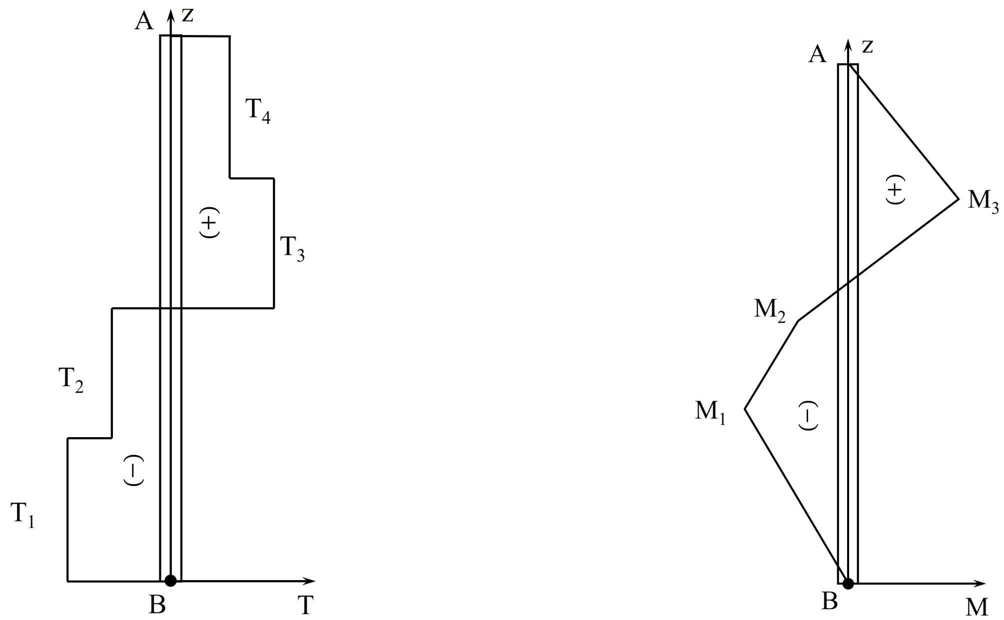

(a) Shear force diagram.

(b) Bending moment diagram.

Fig. 10. Solicitation diagrams of the pin. (a) Shear force distribution. (b) Bending moment distribution.

Table 4. Loading forces and moments values.

Variable	Value
T_1	$\frac{F_x}{2}+\frac{M_y}{L_p}$
T_2	$\frac{F_x}{2}+\frac{M_y}{L_p}-\frac{M_y}{\delta}$
T_3	$\frac{F_x}{2}-\frac{M_y}{L_p}+\frac{M_y}{\delta}$
T_4	$\frac{F_x}{2}-\frac{M_y}{L_p}$
M_1	$\frac{M_y(L_p-\delta)}{2L_p}+\frac{F_x(L_p-\delta)}{4}$
M_2	$\frac{F_x L_p}{4}$
M_3	$\frac{M_y(L_p-\delta)}{L_p}-\frac{F_x(L_p-\delta)}{4}$

In addition, the Navier formula gives the normal stress, as shown below:

$$\sigma=\frac{N}{A}+\frac{My}{I_y} \tag{37}$$

where N is the axial force, A is the cross-sectional area, M is the bending moment, y is the distance from the neutral axis, and I_y is the second moment of area of the section.

On the other hand, the shear stress is approximated for a tubular section as follows:

$$\tau=\frac{4T}{3\pi r^2}\left(1-\frac{y^2}{r^2}\right) \tag{38}$$

where T is the shear force, and r is the radius of the section [103].

In this simplified mechanical model, the pins are made of 38NiCrMo4 steel, whose properties, taken from [104], are presented in Table 5. Therefore, it can be concluded that the pin fails when the Von Mises stress equals its yield tensile stress $\sigma_{y,p}$.

Table 5. Steel 38NiCrMo4 properties.

Material	Density	Elastic Module	Poisson Ratio	Yield Stress	Tensile Strength
Steel 38NiCrMo4	7850 (kg/m^3)	210 (GPa)	0.3 (-)	950 (MPa)	1100 (MPa)

Thus, one has:

$$\sigma_{VM}=\sigma_{y,p}=950\ \text{(MPa)} \tag{39}$$

By combining Equations (36), (38), and (39), a mathematical expression is obtained in which only the section radius r remains unknown. Furthermore, from structural theory [105], it is known that for a circular section, the maximum normal stress occurs at $y=r$, whereas the maximum shear stress occurs at $y=0$. To determine which scenario is most critical, two cases are analyzed. The first assumes failure at $y = r$, whereas the second assumes pin failure at $y = 0$.

For the first case, since $y = r$, the normal stress is maximum, and the shear stress is equal to zero. Consequently, in the first case, Equation (36) leads:

$$\sigma_{VM} = \frac{N}{\pi r^2} + \frac{4M}{\pi r^3} \tag{40}$$

On the other hand, for the second case, where $y = 0$, the normal stress is equal to zero, and the shear stress is maximum. Consequently, in the second case, Equation (36) leads:

$$\sigma_{VM} = \sqrt{\left(\frac{N}{\pi r^2}\right)^2 + 3\left(\frac{4T}{3\pi r^2}\right)^2} \tag{41}$$

Table 6 provides a summary of the radius values obtained for each joint and for each of the cases analyzed in the most critical section of the pin.

Table 6. Pre-dimensions of the section of each pin for the different cases considered.

Component	Case 1 $y = r$	Case 2 $y = 0$
Pin A	r_p = 0.3 (mm)	r_p = 2.2 (mm)
Pin B	r_p = 0.5 (mm)	r_p = 2.9 (mm)
Pin C	r_p = 0.8 (mm)	r_p = 5.4 (mm)

Based on the outcome of the preliminary static analysis carried out above, the proposed initial values for the pin radius are presented in Table 7.

Table 7. Initial values for the radius of each pin.

Component	r_p
Pin A	2.5 (mm)
Pin B	3 (mm)
Pin C	5.5 (mm)

This concludes the pre-dimensioning of the pins performed during the preliminary structural analysis.

3.2.2 Pre-dimensioning of the Arm

The structural arm of the flying car is conceptualized as a hollow tubular beam with a length L_a of 1100 (mm), an outer radius r_o, and an inner radius r_i. The material selected for this study is Aluminum 7075-T6, renowned for its high strength and excellent fatigue resistance, making it an optimal choice for aerospace applications. The mechanical properties of Aluminum 7075-T6, taken from [106], are summarized in Table 8.

Table 8. Aluminum 7075-T6 properties.

Material	Density	Elastic Module	Poisson Ratio	Yield Stress	Tensile Strength
Aluminum 7075-T6	2810 (kg/m^3)	71.7 (GPa)	0.33 (-)	525 (MPa)	572 (MPa)

The objective of this design approach is to optimize the strength-to-weight ratio of the arm while ensuring sufficient rigidity to support the motor and rotor assembly. The tubular section is selected to maximize the moment of inertia, thereby enhancing the resistance of the arm to bending and torsional loads. The preliminary design calculations presented herein determine the values of r_o and r_i based on the applied forces and safety factor requirements.

The arm is modeled as a cantilever beam, as shown in Figure 11, fixed at one end and subjected to a concentrated force F_R at the free end, representing the thrust force generated by the rotor.

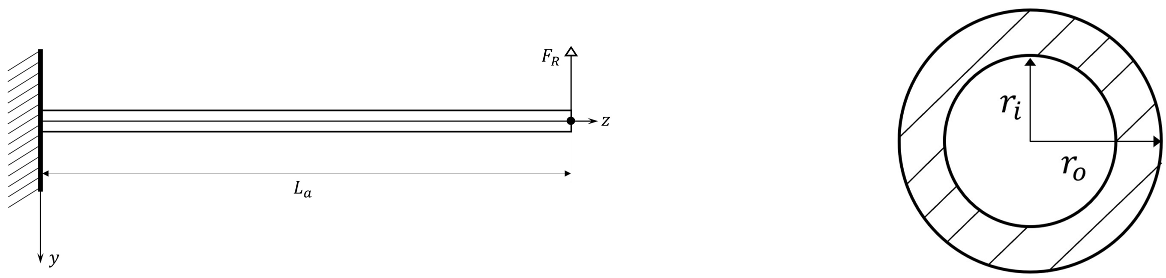

(a) Lateral view of the support arm. (b) Cross section of the support arm.

Fig. 11. Structural scheme of the support arm. (a) Lateral view highlighting the load path and boundary conditions. (b) Cross-sectional configuration of the structural member.

As determined in the previous section and reported in Table 1, the most critical scenario is flight at an angle of 45 degrees, specifically in the rear arm, where a force of 3232.1 (N) is required. As illustrated in Figure 12, the stress diagram shows that the

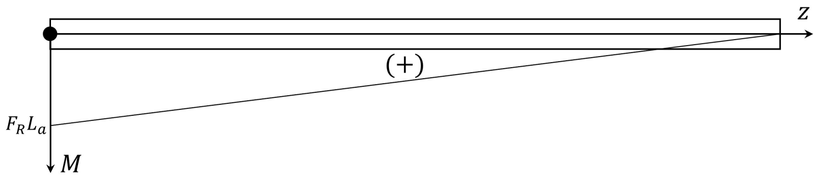

(a) Bending moment diagram.

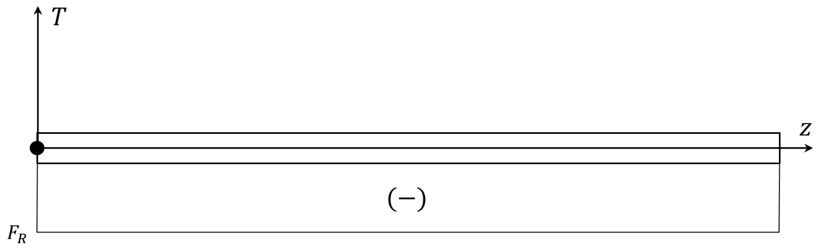

(b) Shear force diagram.

Fig. 12. Solicitation diagrams of the support arm. (a) Bending moment distribution along the structural member. (b) Shear force distribution along the structural member.

most highly stressed point is at the clamped section of the beam, where the moment M equals $F_R L_a$ and the shear T equals F_R. The stress diagram also shows that the stress is highest at the clamped section of the beam.

Upon substituting the aforementioned values into Equation (36), another mathematical expression is obtained that depends solely on the section radius. Because this section has both an inner and an outer radius, a second equation is needed to fully define the system. To this end, a constant arm thickness t_a of 6 (mm) is established, obtained from the following equation:

$$t_a = r_o - r_i \tag{42}$$

For the first case, since $y = r_o$, the normal stress is maximum and the shear stress is equal to zero. Accordingly, for the first case, Equation (36) yields [105]:

$$\sigma_{VM} = \sigma_{y,a} = \sqrt{\left(\frac{4F_R L_a r_o}{\pi(r_o^4 - r_i^4)}\right)^2} \tag{43}$$

where $\sigma_{y,a}$ is the yield stress of the arm, as shown in Table 8. For the second case, where $y = 0$, the normal stress is zero, and the shear stress is maximum. In this case, Equation (36) yields [105]:

$$\sigma_{VM} = \sigma_{y,a} = \sqrt{3\left(\frac{4F_R(r_o^3 - r_i^3)}{3\pi(r_o^4 - r_i^4)t_a}\right)^2} \tag{44}$$

Equations (42), (43), and (44) form a system of two equations with two unknowns, the solution of which determines the inner and outer radii of the arm for the different cases. The numerical values of the geometric parameters, determined using the methodology described here, are presented in Table 9 for reference.

Table 9. Pre-dimensions of the tubular section for the different cases.

Case 1 $(y = r_o)$	Case 2 $(y = 0)$
r_i = 25.4 (mm)	r_i = 2.8 (mm)
r_o = 31.4 (mm)	r_o = 3.2 (mm)

Based on the findings presented in the analysis reported in this section, it is established that the values for arm cross-section indicated in Table 10 should be used as preliminary estimates.

Table 10. Initial values for the arm cross-section.

r_i	r_o	t_a
26 (mm)	32 (mm)	6 (mm)

This completes the preliminary sizing of the arm performed during the preliminary structural analysis.

4. Numerical Results and Critical Discussion

4.1 CAD Model Development

This subsection presents a comprehensive CAD model of the deployment mechanism. The CAD model provides a visual and structural representation of the mechanism, enabling a thorough evaluation of its mechanical feasibility and functionality. By examining the assembly process, component layout, and the integration of key features such as joints, actuators, and locking systems,

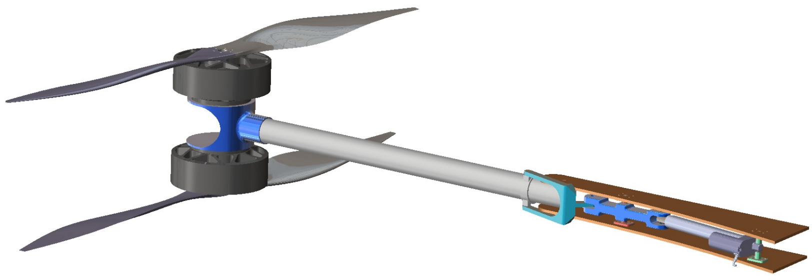

Fig. 13. CAD model of the mechanical components that form the folding mechanism for the propeller support of the flying car that serves as the main case study of the paper.

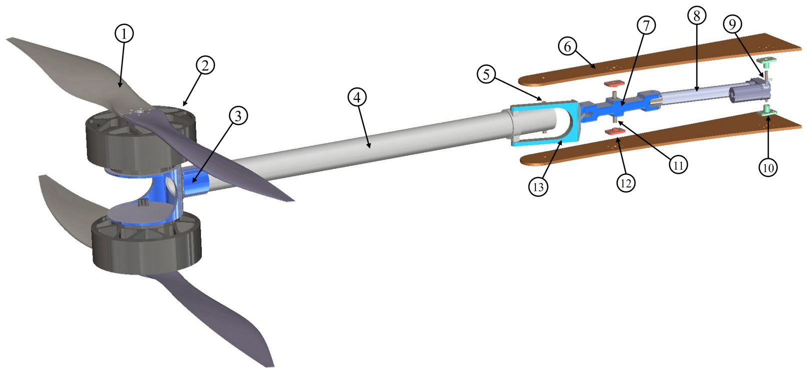

Fig. 14. Exploded view of the mechanical components that form the folding mechanism for the propeller support of the flying car that serves as the main case study of the paper. 1: Propeller, 2: Motor, 3: Motor Support, 4: Arm, 5: Arm Pin, 6: Base, 7: Crank, 8: Actuator, 9: Actuator Pin, 10: Actuator Support, 11: Crank Pin, 12: Crank Support, 13: Connecting Rod.

this section highlights how pre-design considerations translate into a workable solution. To this end, Figure 13 shows the CAD model of the propeller folding mechanism, while Figure 14 presents an exploded view of its distinct components.

Table 11, on the other hand, provides a detailed overview of the components and their proposed construction materials for the system currently under investigation through MBD-FEM analysis.

Table 11. Components and materials of the mechanical parts that form the folding mechanism for the propeller support of the flying car shown in Figure 13.

Item Number	Component Name	Material Type
1	Propeller	Commercial multimaterial subsystem
2	Motor	Commercial multimaterial subsystem
3	Motor Support	Aluminum
4	Arm	Aluminum 7075-T6
5	Arm Pin (Pin C)	Steel 38NiCrMo4
6	Base	Aluminum 7075-T6
7	Crank	Aluminum 7075-T6
8	Actuator	Commercial multimaterial subsystem
9	Actuator Pin (Pin A)	Steel 38NiCrMo4
10	Actuator Support	Aluminum 7075-T6
11	Crank Pin (Pin B)	Steel 38NiCrMo4
12	Crank Support	Aluminum 7075-T6
13	Connecting Rod	Aluminum 7075-T6

4.2 MBD Model Development

The multibody model was developed using MATLAB with the SIMSCAPE MULTIBODY Toolbox [107]. The various components of the mechanism were then incorporated, the interconnections between them were defined, and the external force F_R with magnitude 3232.1 (N), derived in the preceding section, was included. Figure 15 shows the schematic of the multibody model built in SIMSCAPE.

The data for the bodies that serve as mechanical components of the foldable mechanism, including their masses and inertial properties, are given in Table 12.

The local reference frame for each body is located at the center of mass and oriented so that the orientation of the axes is defined to be aligned with the principal inertia directions of each body. In particular, Table 13 presents the spatial information for the center of mass and orientation of each component comprising the propeller folding mechanism.

The provided data includes both translational and rotational components, expressed in the absolute coordinate system defined by the axes x, y, and z. This global reference frame serves as the primary framework throughout the analysis and enables accurate

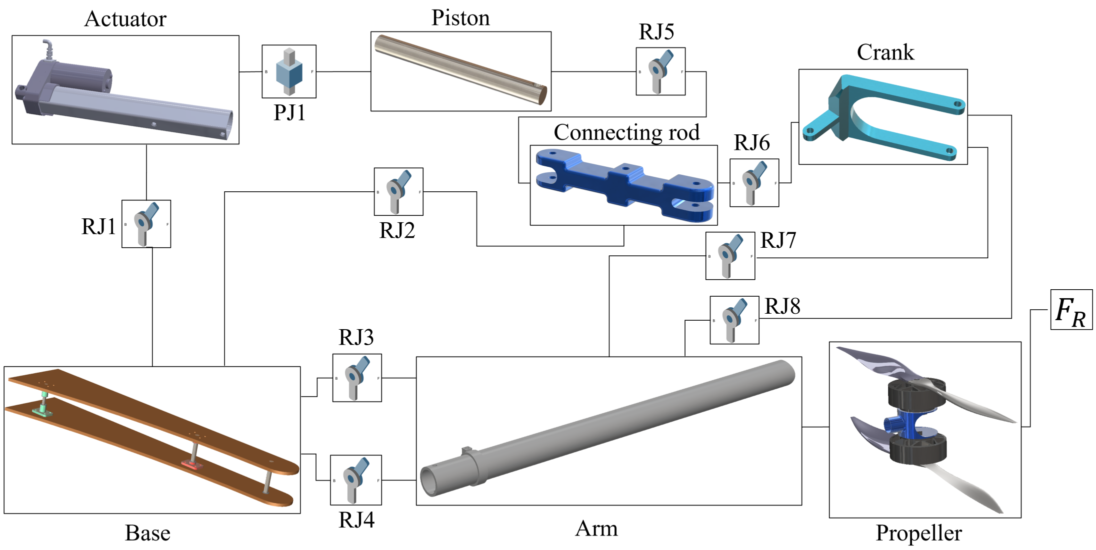

Fig. 15. Multibody model of the closed-chain mechanism that supports and governs the motion of the propeller. RJ: Revolute joint. PJ: Prismatic joint. F_R: Rear propeller force.

Table 12. Mass and inertia properties for the different mechanical components of the propeller folding mechanism.

Body	Mass (m) (kg)	Inertia (I_{xx}, I_{yy}, I_{zz}) (kg×m^2)
Base	3.19	$9.56{\cdot}10^{-3}$, 0.1445, 0.1457
Piston	0.06	$2.21{\cdot}10^{-4}$, $2.21{\cdot}10^{-4}$, $4.46{\cdot}10^{-6}$
Actuator	0.49	$3.11{\cdot}10^{-4}$, $2.04{\cdot}10^{-3}$, $2.23{\cdot}10^{-3}$
Connecting rod	0.77	$2.55{\cdot}10^{-4}$, $3.05{\cdot}10^{-3}$, $3.11{\cdot}10^{-3}$
Crank	0.42	$5.72{\cdot}10^{-4}$, $1.78{\cdot}10^{-3}$, $1.33{\cdot}10^{-3}$
Arm	3.16	$1.03{\cdot}10^{-2}$, 0.2721, 0.2792
Propeller	20	0.8154, 0.1077, 0.7709

Table 13. Location of the center of mass and orientation of each component in the absolute coordinate frame of reference.

Component Name	Translational Coordinates (x, y, z) (m)	Rotational Coordinates (ϕ, ϑ, ψ) (rad)
Base	0.2496, -0.01364, 0	0, 0, 0
Actuator	0.0858, 0.02134, 0	0, 0, 0
Piston	0.2281, 0, 0	0, π/2, 0
Connecting Rod	0.4134, 0.0174, 0	0, 0, 0
Crank	0.5823, 0.079, 0	0, 0, 0
Arm	1.078, 0.1124, 0	0, 0, 0
Propeller	1.645, 0.208, 0	0, 0, 0

delineation of the spatial configuration of each body. Consequently, it facilitates consistent, precise localization of the center of mass and its orientation for all components of the multibody system.

Table 14 presents the localization data for the kinematic joints associated with the different components.

The reported information includes the translational and rotational coordinates needed to position each joint in space. However, it is important to emphasize that both the translational and rotational coordinates in Table 14 are expressed in the local body reference frame of each component. This body-fixed coordinate system, identified by the axes $\bar{x}$, $\bar{y}$, and $\bar{z}$, is the same as the one employed in Table 13, ensuring geometric consistency in how each mechanical component is referenced. Moreover, the rotational orientation of each joint is described using Euler angles denoted by ϕ, ϑ, and ψ, defined following the $X-Y-Z$ sequence of global consecutive rotations. More specifically, when these angles are denoted with a bar, namely $\bar{\phi}$, $\bar{\vartheta}$, and $\bar{\psi}$, they indicate the same sequence of rotations, but measured relative to the local body-fixed reference frame, providing a clear distinction between global and local angular orientations.

Once the MBD model has been constructed, it allows the reactions at the various joints to be calculated. Table 15 presents the calculated reactions at the pins, which are the primary objective of the present analysis.

The coordinate axes referenced in Table 15 are shown in Figure 16, where RJ stands for *Revolute Joint*.

By simulating the mechanism under the most extreme operating condition, the maximum loads the system experiences can be readily captured. These forces represent the most extreme operational stress scenario and serve as the basis for the subsequent finite-element analysis of the pins, which are the most critical components of the deployable mechanism. The next step is to use these reaction forces in a detailed FEA to assess whether the pins, as initially designed in the preliminary dimensioning, can withstand the stresses generated during flight. As a result of the MBD analysis, valuable insights into the system behavior can be

Table 14. Location of the different joints in the body reference system.

Mechanical Component	Kinematic Joint	Translational Coordinates $(\bar{x}, \bar{y}, \bar{z})$ (m)	Rotational Coordinates $(\bar{\phi}, \bar{\vartheta}, \bar{\psi})$ (rad)
Base	RJ1	-0.2496, 0.01364, 0	0, 0, 0
	RJ2	0.1628, 0.03086, 0	0, 0, 0
	RJ3	0.3532, 0.04561, 0.02788	0, 0, 0
	RJ4	0.3532, 0.04561, -0.02938	0, 0, 0
Actuator	RJ1	-0.0858, -0.02136, -4.431$\cdot 10^{-5}$	0, 0, 0
	PJ1	0.2209, -0.02136, 3.499$\cdot 10^{-4}$	0, π/2, 0
Piston	PJ1	1.075$\cdot 10^{-4}$, 0, 0.07859	0, 0, 0
	RJ5	1.075$\cdot 10^{-4}$, 0, 0.07859	0, -π/2, 0
Connecting Rod	RJ2	-1.102$\cdot 10^{-3}$, -1.797$\cdot 10^{-4}$, 3.0554$\cdot 10^{-4}$	0, 0, 0
	RJ5	-0.1067, -0.0174, 0	0, 0, 0
	RJ6	0.09226, 0.01511, 0	0, 0, 0
Crank	RJ6	-0.07618, -0.04649, 0	0, 0, 0
	RJ7	0.1104, -0.01063, -0.045	0, 0, 0
	RJ8	0.1104, -0.01063, 0.045	0, 0, 0
Arm	RJ3	-0.4757, -0.08042, 0.02819	0, 0, 0
	RJ4	-0.4757, -0.08042, -0.02907	0, 0, 0
	RJ7	-0.3858, -0.04401, -0.045	0, 0, 0
	RJ8	-0.3858, -0.04401, 0.045	0, 0, 0
	Fixed	0.5666, 0.09561, 0	0, 0, 0
Propeller	Fixed	-0.5666, -0.09561, 0	0, 0, 0

Table 15. Reaction values on the different pins obtained through the MBD model. The values of all reaction forces and moments are computed in the reference systems of the corresponding mechanical joints.

Component	Joint	Reaction	$\bar{x}$ axis	$\bar{y}$ axis	$\bar{z}$ axis
Pin A	RJ_1	Force (N)	0	2.5	149.8
		Moment (N$\times$m)	42.7	-291.2	0
Pin B	RJ_2	Force (N)	-7755	-1407	630.6
		Moment (N$\times$m)	128.2	-780.2	0
Pin C	RJ_3	Force (N)	3844	783	1140
		Moment (N$\times$m)	192.3	-1174	0
	RJ_4	Force (N)	3911	794	1140
		Moment (N$\times$m)	192.3	-1174	0

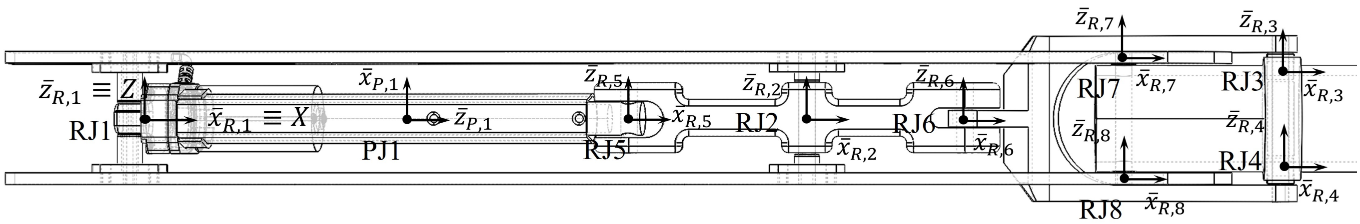

Fig. 16. Coordinate axes and location of the revolute joint of the pins in the MBD analysis. RJ: Revolute joint. PJ: Prismatic joint.

gained, enabling a precise evaluation of the structural integrity of the most critical components. To achieve the goals mentioned earlier, the fundamental parameters of the numerical solver employed in this paper are reported in Table 16.

Table 16. Fundamental parameters of the numerical solver used in MATLAB and in SIMSCAPE MULTIBODY.

Description	Symbol	Value (Units)
Dynamical simulation time span	T_s	5 (s)
Dynamical simulation time step	Δt	10^{-3} (s)
Solver relative error tolerance	ε_r	10^{-8} (m) or (rad)
Solver absolute error tolerance	ε_a	10^{-11} (m) or (rad)

In Table 16, T_s and Δt represent the simulation time span and time step, respectively, while ε_r and ε_a represent the relative and absolute error tolerances of the numerical solver, respectively. Although a dynamic analysis has been conducted using the settings reported in Table 16, it is worth emphasizing that the external load has been applied statically to the multibody model of the mechanical system under study to focus the computer simulation results on the most severe loading scenario.

4.3 Comparative Analysis and Discussion

This subsection presents three proposed methods for transferring the reactions from the MBD simulation into the finite element model for the structural analysis of the pins in the foldable support mechanism of the flying car propeller. The primary objective is to evaluate the performance of the pins under critical loading conditions derived from the MBD model. The MBD analysis yields forces and moments at the pin interfaces, which must be accurately transferred into the finite element environment for detailed stress analysis.

This study examines three distinct pin-related subsystems: A) the pin-actuator system, B) the pin-crank system, and C) the pin-arm system. As illustrated in Figure 17, these subsystems differ in their mechanical configurations and load transmission paths, which influence their respective stress distributions.

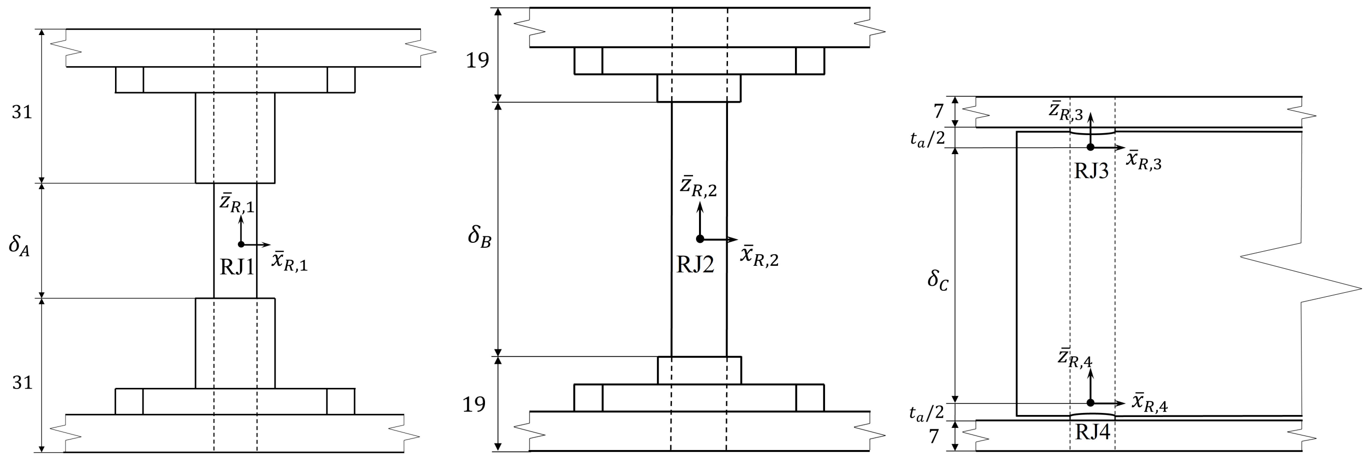

(a) Pin A: pin–actuator system. (b) Pin B: pin–crank system. (c) Pin C: pin–arm system.

Fig. 17. Assembly configurations of the pin connection systems. (a) Pin–actuator system. (b) Pin–crank system. (c) Pin–arm system. The geometric displacements δ_A, δ_B, and δ_C are obtained from the kinematic relationships and are equal to 18 mm, 42 mm, and 54 mm, respectively.

Each of these systems is analyzed using the three proposed methodologies for transferring loads from MBD to FEM. The effectiveness of each method is assessed by comparing stress distributions and identifying potential stress concentration zones in the pins. The objective is to determine the most precise and realistic approach for transferring loads between simulation environments while ensuring the structural integrity of the pins under operational conditions.

4.3.1 Direct Reactions Method (DRM)

The Direct Reactions Method (DRM) applies the forces and moments derived from the MBD analysis directly to the FEM model. In this approach, the reaction loads and moments are applied to a master node at the geometric center of the pin. The pin surface is then connected to this master node via a rigid constraint, ensuring that the applied loads are uniformly distributed across the structure. The pin region in contact with the supporting components is fully constrained to replicate the mechanical constraints in the assembly. This method provides a straightforward and computationally efficient way to transfer loads from MBD to FEM. However, the accuracy of this method depends on the assumption that the applied loads are uniformly distributed across the rigid link to the pin surface. The outcome of this method is shown in Figure 18.

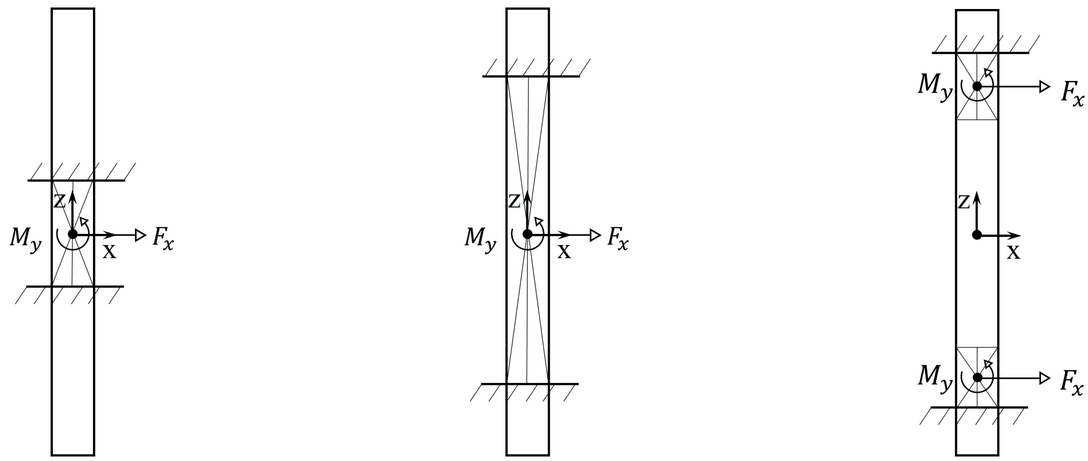

(a) Pin A: pin–actuator system. (b) Pin B: pin–crank system. (c) Pin C: pin–arm system.

Fig. 18. Two-dimensional schematization of the Direct Reactions Method (DRM) used to transfer reaction forces from the multibody dynamics (MBD) model to the finite element model (FEM). (a) Actuator pin configuration. (b) Crank pin configuration. (c) Arm pin configuration.

As illustrated in Figure 18, this method is outlined for three distinct pin configurations. Each case follows a consistent procedure, with the master node located at the pin center and reaction forces and moments applied directly. The effectiveness of this method is evaluated by its ability to capture stress distributions and critical load-bearing regions within the pin structures.

4.3.2 Moments Transformation Method (MTM)

The Moments Transformation Method (MTM) is a refinement of the Direct Reactions Method that addresses its limitations by improving the treatment of applied moments. In this approach, forces and moments from the MBD model are applied via a master node attached to the pin surface. Instead of applying moments as rotational loads, they are transformed into equivalent shear forces distributed across the pin contact surface. This transformation eliminates bending moments from the analysis, ensuring that the pins are subjected only to axial and shear stresses, which better reflect their actual mechanical function. The forces remain applied through the master node, ensuring consistent load transfer.

Furthermore, in the Moments Transformation Method (MTM), the boundary conditions differ from those of the previous method. Rather than fully constraining the pin at its interface with the support, only the upper and lower sections of the pin are fixed. To account for the actual influence of the support, the reaction forces generated by the support due to the applied loads are calculated and applied as a distributed force over the corresponding surface.

Figure 19 illustrates the application of the transformed shear stresses and support reaction forces, providing a more accurate representation of the actual loading conditions.

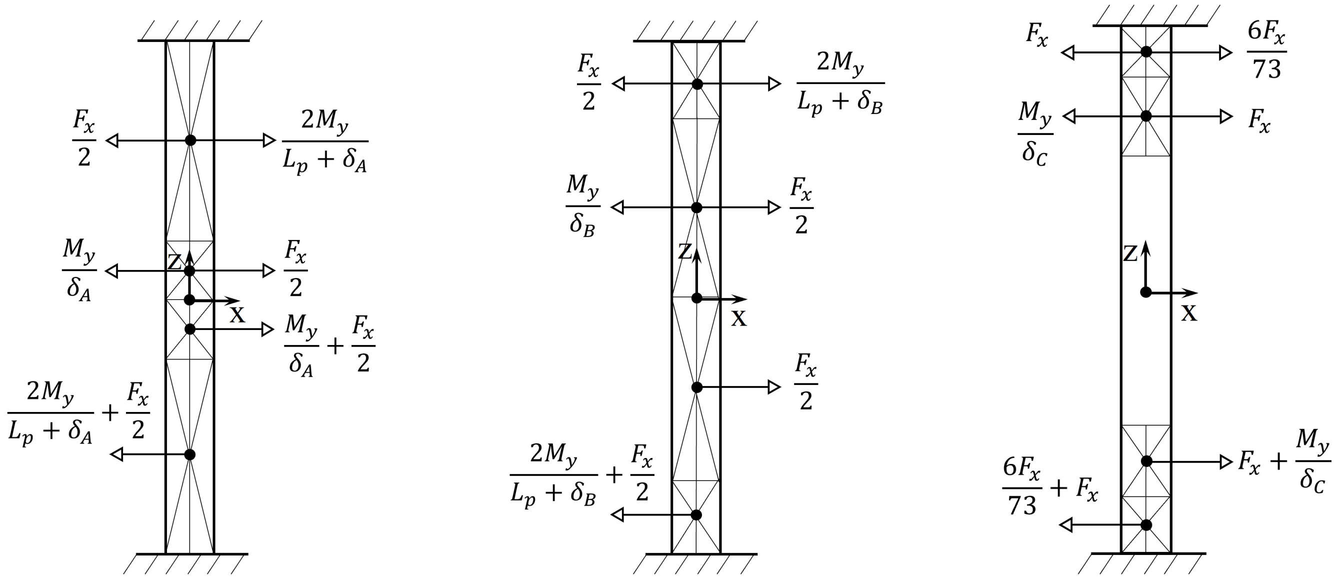

(a) Pin A: pin–actuator system. (b) Pin B: pin–crank system. (c) Pin C: pin–arm system.

Fig. 19. Two-dimensional schematization of the Moments Transformation Method (MTM) used to transfer reaction loads from the multibody dynamics (MBD) model to the finite element model (FEM). (a) Actuator pin configuration. (b) Crank pin configuration. (c) Arm pin configuration.

In the Moments Transformation Method (MTM), forces are applied directly to the pin surface rather than transmitted through a single master node. This approach more accurately reflects the actual load distribution in a physical setting, as the pin surface experiences a distributed load rather than a concentrated point load. Furthermore, the reactions at the upper and lower extremities of the pin, where the pin interfaces with its supports, are calculated based on the distributed forces. Subsequently, these reactions are applied as distributed forces over the top and bottom surfaces of the pin, rather than assuming rigid fixation, as in the initial method.

This approach permits a more realistic representation of the boundary conditions, as the pin is permitted to deform slightly in response to the applied loads, and the stresses are distributed more evenly across the contact surfaces. Although this method provides a more accurate representation of the load distribution and eliminates the unrealistic application of moments, concerns remain regarding stress concentrations. The use of master nodes for load distribution may still result in localized areas of high stress, particularly in regions where forces are applied. This can lead to an overestimation of stress levels in these areas, though to a lesser extent than in the first method. However, the deformation behavior of the pin is more realistic in this case, and the stress distribution is closer to what would be observed in practice.

4.3.3 Loads Distribution Method (LDM)

The third and final method, called the Loads Distribution Method (LDM), builds on the enhancements of the second method while further refining the approach to eliminate the use of master nodes entirely. In contrast to the previous method, which applied forces to the surface of the pin linked to a master node, this method applies pressure loads derived by dividing the total force from the MBD simulation by the contact area over which it is applied. The radii for the different pins are shown in Table 7. This approach applies the load directly as pressure over the pin surface, rather than as discrete forces at specific points. Applying uniform pressure across the pin surface provides a more accurate representation of how the load would be transmitted through the component in a real-world scenario. Furthermore, the moments from the MBD model are again converted into shear stresses, which are then applied as pressures over the relevant surfaces. The reactions at the top and bottom of the pin, which simulate the support conditions, are also applied as pressures. This ensures that the loads are distributed evenly over the surfaces, rather than concentrated at specific points, as depicted in Figure 20.

All the loads shown in Figure 20 are intended to be transformed into pressures distributed across the respective sections of the cylindrical surfaces to which they are applied. Eliminating master nodes and applying loads as pressures yield a more realistic simulation of the pin behavior under its actual loading conditions based on the Loads Distribution Method (LDM).

The stress concentrations in the first two methods are significantly reduced because the loads are now distributed more naturally across the surface of the pin. This results in a more accurate prediction of the stress distribution and deformation of the pin, providing reliable data for evaluating the structural integrity of the component. Moreover, by transforming the moments into shear stresses

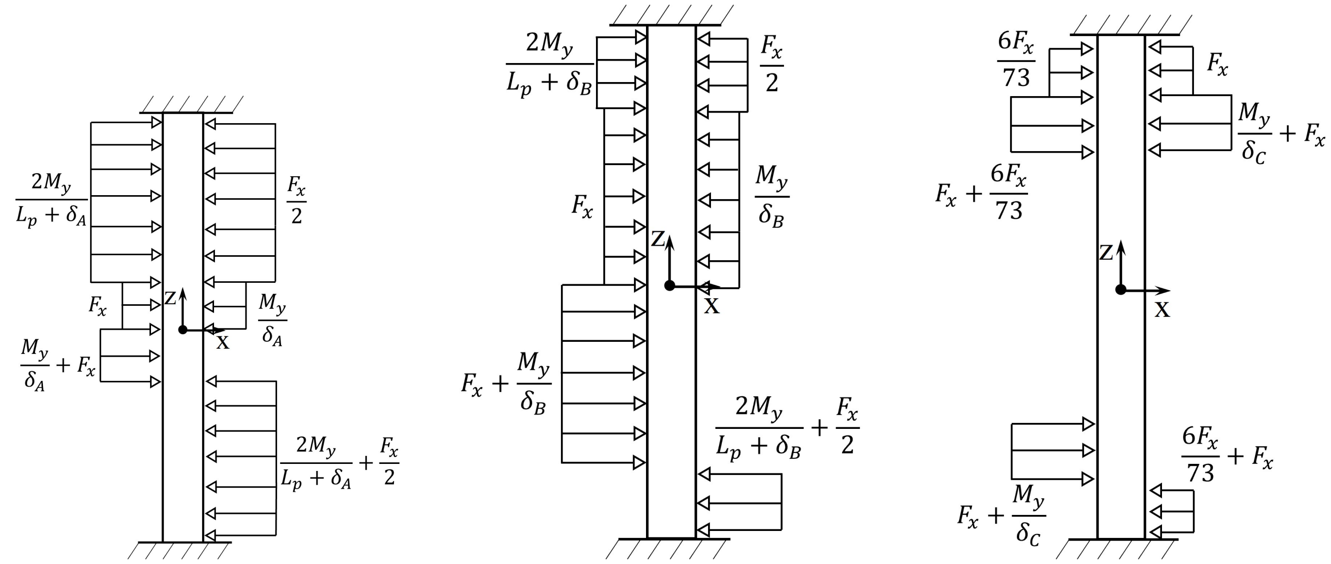

(a) Pin A: pin–actuator system. (b) Pin B: pin–crank system. (c) Pin C: pin–arm system.

Fig. 20. Two-dimensional schematization of the Loads Distribution Method (LDM) used to transfer reaction loads from the multibody dynamics (MBD) model to the finite element model (FEM). (a) Actuator pin configuration. (b) Crank pin configuration. (c) Arm pin configuration.

and applying them as pressures, this method circumvents the implausible application of moments that was problematic in the initial method. The pin is subjected to the types of loads for which it is designed, and the boundary conditions at its top and bottom are more accurately represented by applying distributed pressures rather than rigid constraints.

4.3.4 Comparison of Methods Performance

As discussed above, three computational methods were used in this investigation to analyze the strength of the most vulnerable pin components of the opening mechanism, namely 1) the Direct Reactions Method (DRM), 2) the Moments Transformation Method (MTM), and 3) the Loads Distribution Method (LDM). After evaluating the three methods, it is evident that the third method, the Loads Distribution Method (LDM), is the most physically representative approach among the three strategies considered in this study for transferring the reactions from the MBD simulation to the FEM model.

The first method, which applies all reactions to a single master node and enforces rigid boundary conditions, produces implausible stress concentrations and fails to accurately reflect the behavior of the pins under load. The second method improves on the first by eliminating moments. However, the use of master nodes still introduces localized high-stress regions. In contrast, the third method, which applies loads as pressures, provides the most realistic simulation of the pin behavior. Removing master nodes and applying distributed pressures rather than concentrated forces result in a more uniform stress distribution, thereby reducing the probability of artificially elevated stress concentrations. Transforming moments into shear stresses and applying them as pressures further enhances the accuracy by ensuring that the pins are subjected to the loads they are designed to handle.

A comparative analysis of the three proposed methodologies for transferring the reactions from the MBD analysis to the FE model was conducted. To this end, the pin-crank system case was used, with the pin section radius assumed to be 5 (mm), and the applied loads summarized in Table 17.

Table 17. Applied loads for the pin in the comparative analysis. The values of all reaction forces and moments are calculated in the global reference systems utilized in the finite element analysis, which align with the mechanical joint reference frames.

Reaction	$\bar{x}$ axis	$\bar{y}$ axis	$\bar{z}$ axis
Force (N)	-7755	-1407	630.6
Moment (N$\times$m)	128.2	-780.2	0

The results of the comparative analysis of the three methods are illustrated in Figure 21, which shows the Von Mises stress contours for each case.

As illustrated in Figure 21, the third method, referred to as the Loads Distribution Method (LDM), yields stress distributions that are markedly more uniform and free of the stress concentrations observed in the other two methods. This finding corroborates the assertion that the third method is the most suitable for simulating the behavior of the pin under load. This method is the most physically representative of the three load-transfer strategies considered in this study. In light of these findings, all subsequent analyses will utilize the third method to ensure the most accurate and reliable results.

To ensure the accuracy and reliability of the finite element results, a rigorous mesh-independence study was conducted before the final evaluations. Successive refinements of the quadratic tetrahedral mesh were applied to the critical components until the maximum Von Mises stress and deformation converged. This confirms that the reported structural responses are independent of the grid resolution. Although the LDM is regarded as the most realistic simulation technique because it mitigates artificial stress concentrations, it also entails higher computational costs than the DRM and MTM. Applying varying pressure distributions across the pin contact surfaces in the LDM requires additional preprocessing time and marginally increases the solver's convergence time. However, this computational trade-off is well justified by the significant gains in simulation fidelity and the prevention of overly conservative, oversized mechanical designs.

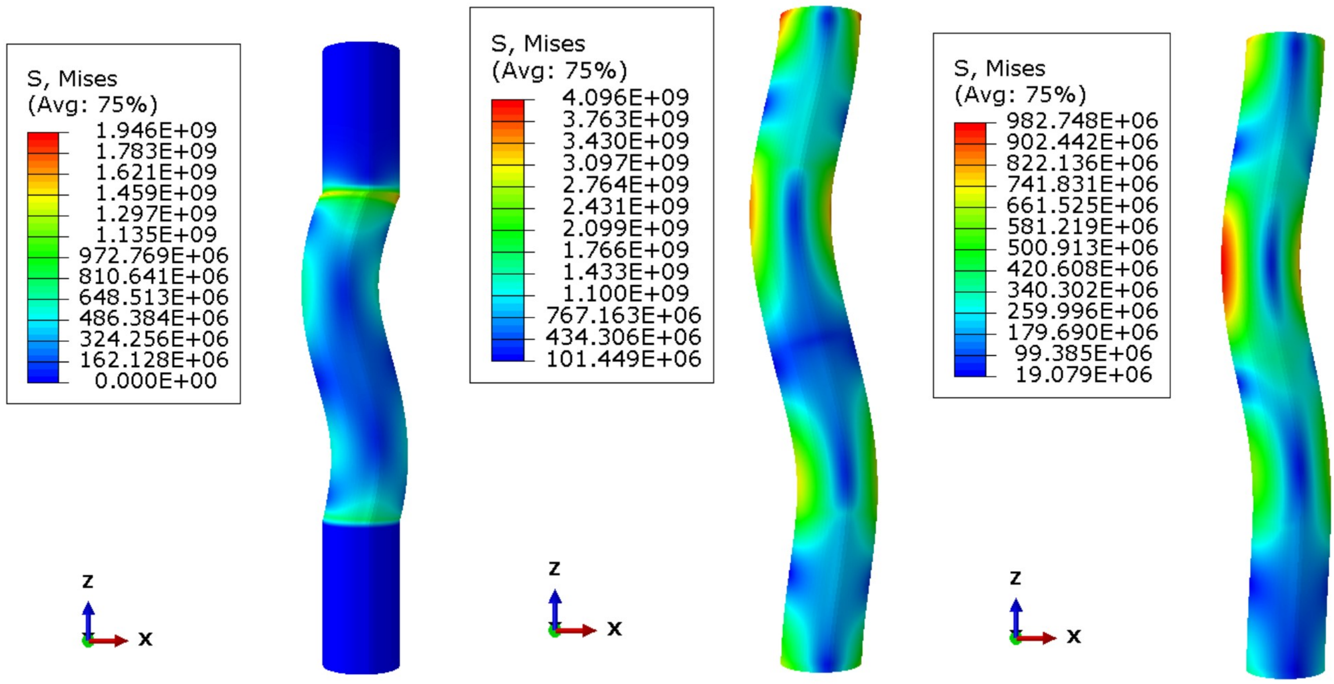

(a) Direct Reactions Method. (b) Moments Transformation Method. (c) Loads Distribution Method.

Fig. 21. Von Mises stress contour plots obtained using the three load transfer methodologies. (a) Direct Reactions Method (DRM): direct application of reaction forces and moments at the master node. (b) Moments Transformation Method (MTM): direct application of reaction forces at the master node with transformation of reaction moments into equivalent shear forces. (c) Loads Distribution Method (LDM): transformation of reaction forces and moments at the master node into equivalent distributed pressure loads.

4.4 FEM Model Development and Structural Results Comparison

In this subsection, an FE analysis is conducted using the third methodology discussed earlier, the Loads Distribution Method (LDM), which was shown to yield results that most closely resemble real-world conditions. The pins are analyzed using the dimensions from the preliminary sizing phase and under the previously described loading conditions. These dimensions and loads are presented in Tables 7 and 15, respectively. By applying distributed pressure to the pin surfaces as described, the resulting stress distributions within the pins are made as realistic as possible.

To formally quantify the comparative performance of the load-transfer strategies, the maximum stress values and their corresponding relative deviations are presented in Table 18.

Table 18. Quantitative comparison and error analysis of the maximum Von Mises stress across the three proposed load-transfer methods.

Methodology	Maximum Von Mises Stress (MPa)	Relative Deviation versus the LDM results (%)
DRM (Direct Reactions)	1946.00	98.02%
MTM (Moments Transformation)	4096.00	316.79%
LDM (Loads Distribution - Ref.)	982.75	–

Since the LDM approach provides the most physically representative load-transfer mechanism, it was adopted as the benchmark for quantitative comparison. The numerical data in Table 18 show that the DRM and MTM methodologies yield peak stress values that are 98.02% and 316.79% higher than the LDM benchmark, respectively. These substantial discrepancies indicate that although simpler methods such as DRM and MTM may capture the general stress pattern, they fail to provide the localized accuracy required for aerospace components because they introduce nonphysical stress singularities at the application points. Consequently, the quantitative evidence supports the LDM as the most accurate and reliable technique for the preliminary high-resolution structural assessment of the deployable support system.

Although the LDM produces lower maximum Von Mises stresses than the DRM and MTM, this lower level should not be interpreted simply as a conservative or nonconservative result. Rather, it reflects the removal of artificial stress concentrations caused by concentrated load application. To ensure mechanical consistency, the distributed pressures used in the LDM must preserve the resultant forces and moments obtained from the MBD model. Therefore, the pressure fields applied in the finite element model are selected so that their integrals over the loaded surfaces reproduce the corresponding MBD joint reactions. This equilibrium-preserving condition is essential for a meaningful transfer of loads from the multibody model to the finite element model.

The present structural analysis focuses on the three most critical pins in the folding and unfolding mechanism, as these components are subjected to the highest loads during operation. The results of the Von Mises stress analysis for the three pins are illustrated in Figure 22.

The stress contours shown in Figure 22 provide a visual representation of the stress distribution across the pin surfaces under critical loading conditions. Upon examination of these contours, it becomes evident that the maximum stress levels occur at specific points along the pin surfaces, particularly at points of interaction with adjacent components, such as the crank arms or support plates.

In addition, the safety factor η for each pin is calculated using the Von Mises stress results. The safety factor is determined by comparing the maximum stress values obtained from the FEM analysis with the yield strength $\sigma_{y,p}$ of the material utilized for the

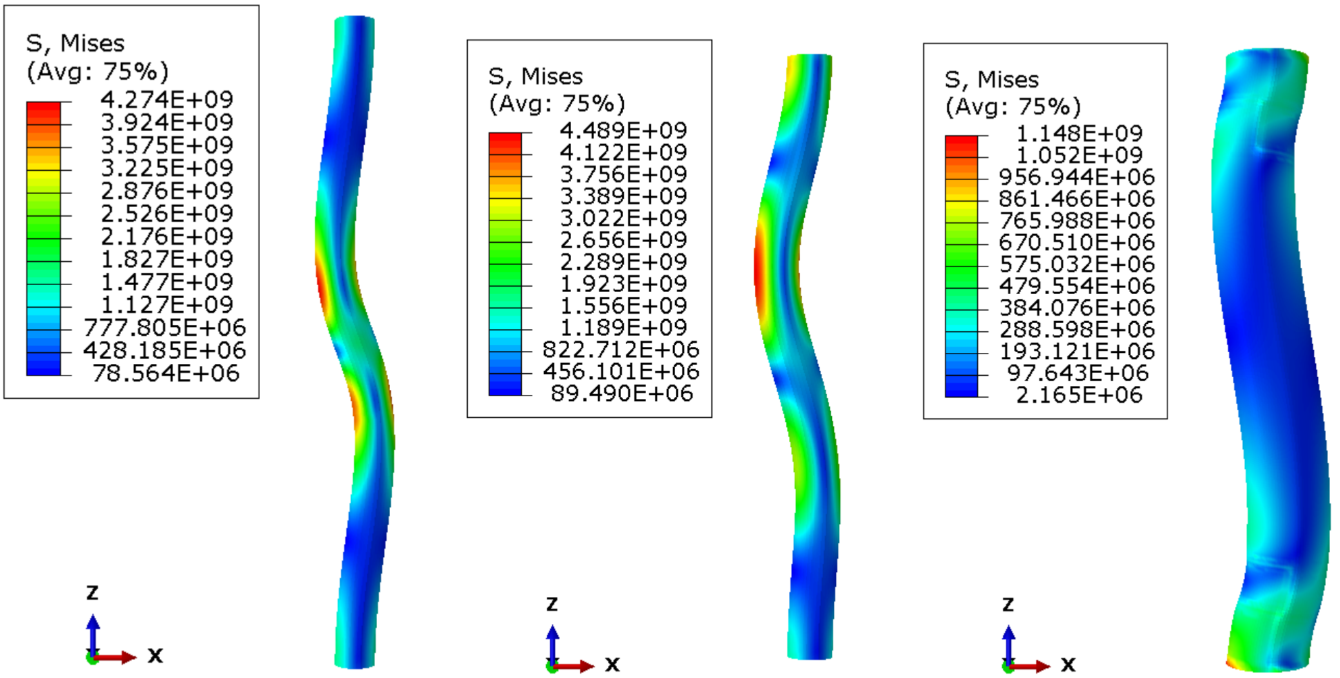

(a) Pin A: pin–actuator system. (b) Pin B: pin–crank system. (c) Pin C: pin–arm system.

Fig. 22. Von Mises stress contour plots for the initial pin geometries obtained using the Loads Distribution Method (LDM). (a) Actuator pin configuration. (b) Crank pin configuration. (c) Arm pin configuration.

pins, as shown below:

$$\eta = \frac{\sigma_{y,p}}{\sigma_{VM}} \tag{45}$$

The calculated safety factors for each of the three pins are presented in Table 19.

Table 19. Safety factor for the pins under the applied loading conditions.

Component	Safety factor η (-)
Pin A	0.22
Pin B	0.21
Pin C	0.83

As shown in Equation (45), a safety factor greater than one is typically deemed sufficient to ensure that the element in question can withstand the forces to which it is subjected. In the specific instance under consideration, however, a more rigorous standard is being applied, requiring a safety factor greater than or equal to 1.5 (-).

An inspection of the results in Table 19 shows that none of the pins meet the requisite safety standards under the current design. The safety factors for all three pins fall below the minimum acceptable value, indicating that the preliminary sizing dimensions are insufficient to withstand the critical loads they are subjected to. This indicates that resizing of all three pins is necessary to meet the structural requirements and ensure the safe operation of the folding mechanism.

Given the inadequacy of the current pin dimensions, an iterative optimization process will be conducted in the next section. In this process, the diameter of each pin will be adjusted, and the MBD simulation will be rerun to update the load conditions. Subsequently, the finite element analysis will be repeated to verify that the new dimensions can resist the applied forces and stresses. This iterative approach will continue until all pins have been verified and can withstand the loads with a satisfactory safety factor.

After each geometric modification, the finite element analysis is repeated to verify the updated stress distribution and safety factor. In the present static worst-case analysis, the MBD joint reactions are held constant because the external thrust, the mechanism's open configuration, and the kinematic constraint layout remain unchanged. Therefore, the same reaction loads from the MBD model are used for iterative FEM-based resizing. If the redesign's variations in mass and inertia are accounted for in a fully dynamic deployment simulation, the MBD model should be updated accordingly.

In addition to the pin analysis, an FE analysis is conducted for the arm component. The initial dimensions of the arm are provided in Table 10. Unlike the pins, no load transformation is required in this case. The arm is directly subjected to the loads from the motors, which are applied at the tip, while the arm is fixed at its opposite end. The applied load corresponds to the critical flight condition at 45 degrees, and the load value is provided in Table 1 for reference. Figure 23 illustrates the FE setup for the arm, which is constrained at one end and subjected to a load at the tip.

This configuration ensures that the model accurately replicates the mechanical behavior of the supporting arm under these flight conditions. Furthermore, the Von Mises stress contours reveal regions of maximum stress concentration. The stress distribution from the initial FEM analysis is illustrated in Figure 24.

Following the initial FEM analysis, the safety factor for the arm was calculated and is presented in Table 20.

Although the safety factor is greater than 1, indicating that the arm can withstand the applied load, it is below the required threshold of 1.5. As noted earlier, a safety factor of at least 1.5 provides an initial static design margin. However, it does not eliminate the need for fatigue verification in later design stages. Therefore, the existing arm design is inadequate and must be redesigned

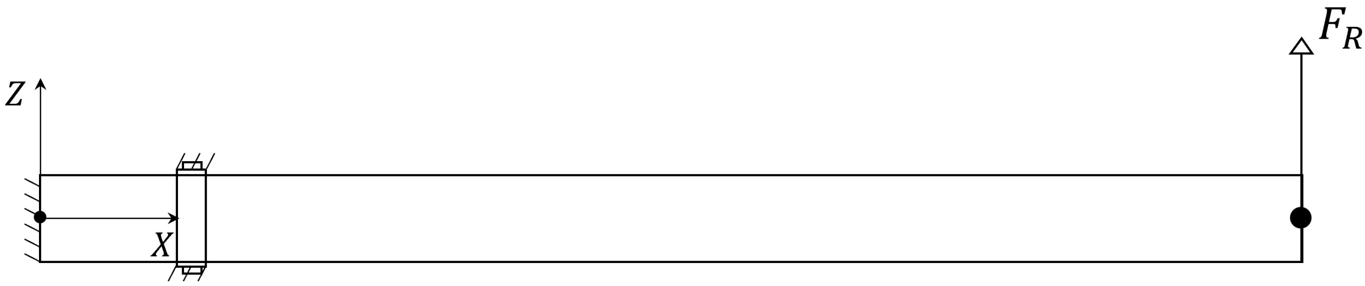

Fig. 23. Two-dimensional schematization of the boundary conditions and loads applied to the support arm.

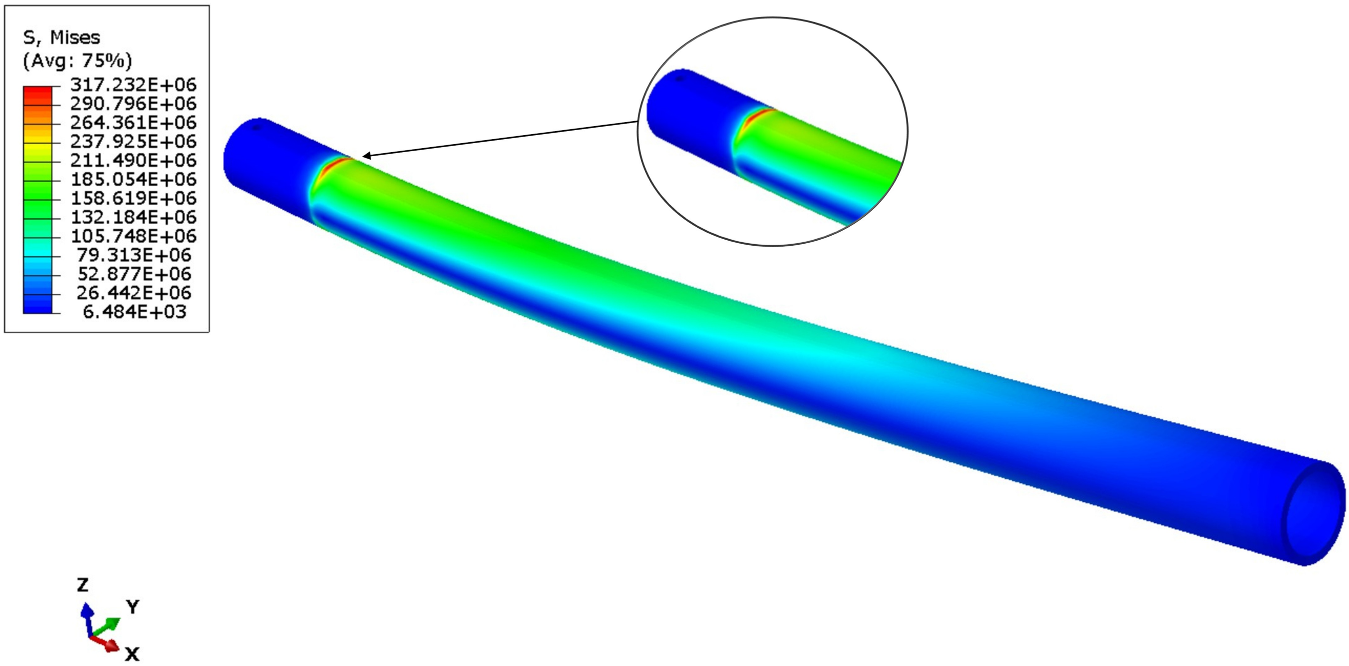

Fig. 24. Von Mises stress contour plot for the support arm with the initial geometric dimensions.

Table 20. Safety factor for the arm under the applied loads.

Component	Safety factor η (-)
Arm	1.34

to meet the requisite safety margin. To achieve this, the external radius of the arm r_o will be maintained at 32 (mm), while the internal radius will be adjusted iteratively by increasing the wall thickness. Following each modification, the MBD simulation will be rerun to determine the new reaction forces, and the FEM analysis will be repeated until the safety factor reaches the required value. This iterative design process will be covered in detail in the next subsection.

To ensure the structural reliability of the foldable mechanism under the stringent requirements of Urban Air Mobility, a factor of safety of 1.5 has been adopted for all critical components. This value is not arbitrary but strictly aligns with Federal Aviation Administration (FAA) standards in Federal Aviation Regulation (FAR) Part 27.303, which requires a factor of safety of at least 1.5 for aircraft structural designs unless otherwise specified [101]. This margin ensures that the deployable support can withstand limit loads without permanent deformation and ultimate loads without catastrophic failure during the transition phases. Furthermore, the operational lifespan of such aerospace mechanisms is heavily influenced by High-Cycle and Low-Cycle Fatigue (HCF/LCF). However, the present study is strictly limited to the preliminary static design and proof-of-concept phase of the integrated CAD-MBD-FEM framework. Comprehensive spectral fatigue analysis, including vibration-induced degradation and ultimate limit state testing under cyclic loading, is outside the current scope and will form the core of the second-version prototype development and experimental validation.

4.5 Iterative Design Improvement

The objective of this subsection is to enhance the geometric characteristics of both the pins and the arm to ensure they meet the safety factor requirements previously outlined. For the pins, the radius r_p increases gradually while the length remains constant. For the arm, the section thickness t_a is increased and the internal radius r_i is decreased, while the outer radius r_o is intentionally kept constant. This approach allows the mechanical resistance of each component to be adjusted without significantly altering its overall dimensions. It is crucial to note that the MBD analysis remains unchanged throughout this iterative process. The geometric modifications do not affect the overall reaction forces and moments within the system. Consequently, the loads applied in the previous analysis, as outlined in Table 15, remain valid for the new geometries. Consequently, the reactions in the MBD model remain unchanged, and the sole variable that changes is the structural response resulting from the modified dimensions.

The iterative design process begins by increasing the diameter of each pin and decreasing the internal radius of the arm until the safety factor is at least 1.5. The final Von Mises stress contours for the optimized geometries of the pins and the arm are shown in Figures 25 and 26, respectively.

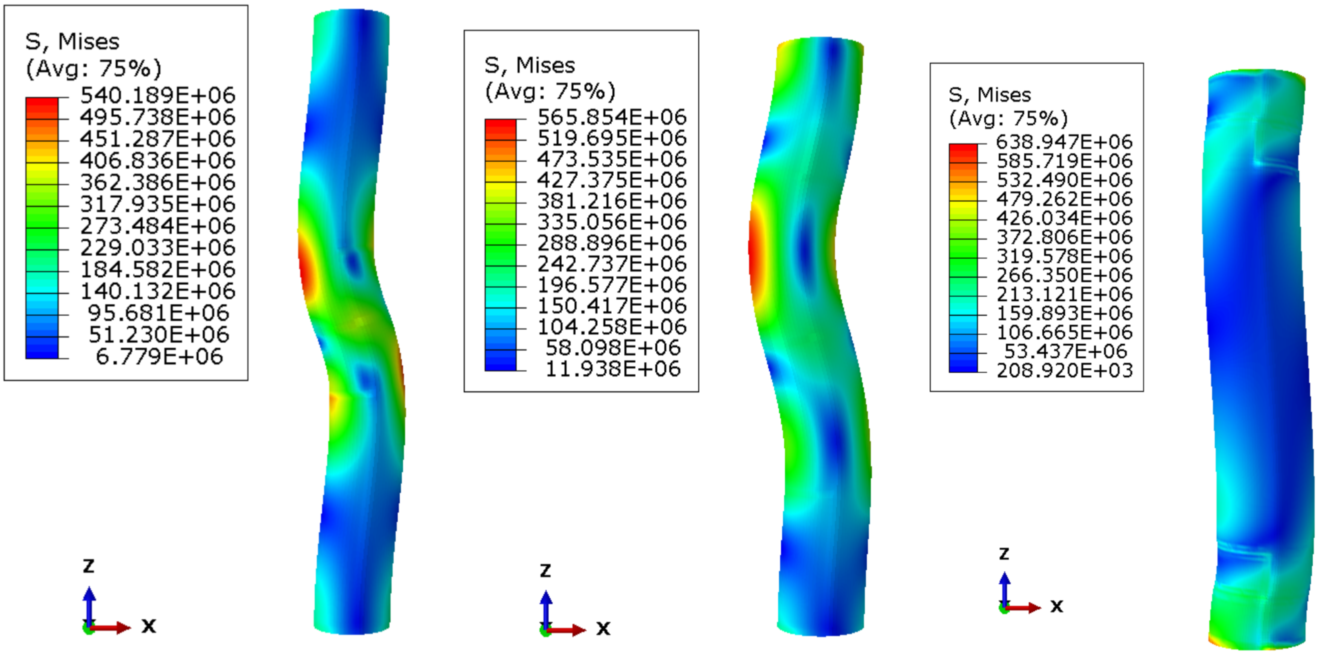

(a) Pin A: pin–actuator system.

(b) Pin B: pin–crank system.

(c) Pin C: pin–arm system.

Fig. 25. Von Mises stress contour plots for the final optimized pin geometries obtained after the iterative design procedure. (a) Optimized actuator pin. (b) Optimized crank pin. (c) Optimized arm pin.

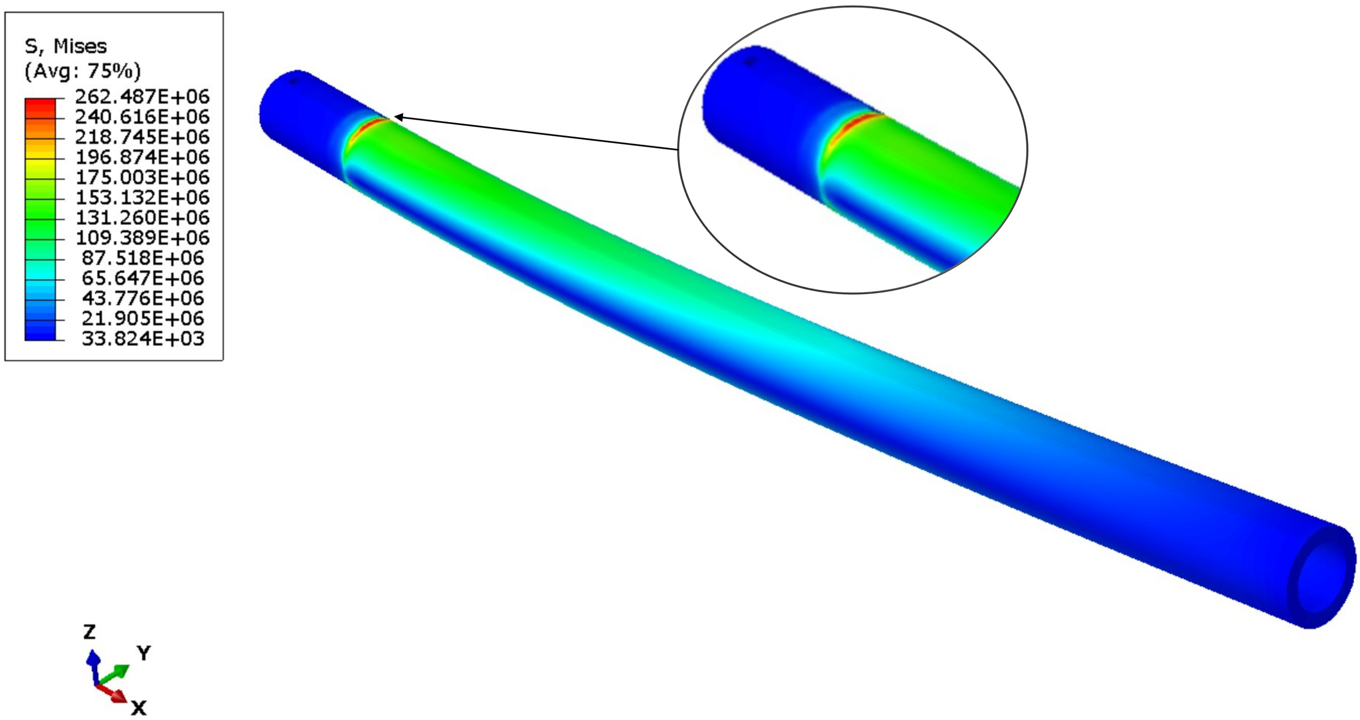

Fig. 26. Von Mises stress contour plot for the final optimized arm geometry.

Additionally, Table 21 lists the safety factors for each component after the iterative design improvements.

Observing Table 21, it can be seen that all safety factors are now greater than or equal to 1.5, confirming that the redesigned components meet the required safety margins.

Table 22 provides a summary of the initial dimensions from the preliminary design stage and the final dimensions that meet the established criteria for both the arm and the three pins.

The iterative process presented here ensured that all components were carefully optimized to meet structural requirements under critical load conditions, resulting in an optimal design for the case study examined in this paper.

For the current structural validation, it is essential to define the boundaries of the mission profile under analysis. Although the operational environment of UAM vehicles encompasses a wide array of critical load cases, including aerodynamic gusts during maneuvers, transient impact forces during folding and deployment sequences, and cyclic fatigue over the service life, the scope

Table 21. Final safety factors for the optimized pins and arm after iterative design.

Component	Safety factor η (-)
Pin A	1.75
Pin B	1.68
Pin C	1.50
Arm	1.62

Table 22. Summary of initial dimensions from preliminary design and final optimized dimensions for pins and arm.

Component	Initial dimension	Final dimension
Pin A	$r_p = 2.5$ (mm)	$r_p = 5$ (mm)
Pin B	$r_p = 3$ (mm)	$r_p = 6$ (mm)
Pin C	$r_p = 5.5$ (mm)	$r_p = 7$ (mm)
Arm	$r_i = 26$ (mm)	$r_i = 22$ (mm)
	$r_o = 32$ (mm)	$r_o = 32$ (mm)
	$t_a = 6$ (mm)	$t_a = 10$ (mm)

of this initial research phase is strictly focused on proof-of-concept and the static structural feasibility of the mechanism. The hovering condition is selected as the baseline load case because it represents a sustained, high-power-demand state with constant force transmission, providing a reliable metric for the initial assessment of the CAD-MBD-FEM integrated framework. Achieving full aerospace maturity will require incorporating high-fidelity transient phenomena. Consequently, integrating complex aerodynamic load profiles and transitioning to multibody dynamic analysis involving flexible bodies are formally categorized as core objectives of the subsequent phase of prototype development. This phased approach allows for the systematic elimination of kinematic risks before committing to the computationally intensive aero-elastic simulations required for final certification.

Furthermore, Table 21 shows that all safety factors are at least 1.5, confirming that the redesigned components meet the required safety margins. Table 22 summarizes the initial dimensions from the preliminary design stage and the final dimensions that meet the established criteria for both the arm and the three pins. To address the inherent trade-off between structural strength and weight efficiency, a paramount consideration in UAM applications, a comparative mass analysis is presented in Table 23.

Table 23. Mass-versus-safety-factor trade-off analysis across the preliminary and the optimized design phases.

Design Phase	Total System Mass (kg)	Minimum Safety Factor (-)	Relative Change (%)
Preliminary Design	25.37	0.22	—
Optimized Design	27.34	1.50	7.77

The optimization process, which involved increasing the pin radii and reducing the internal radius of the tubular arm to increase its cross-sectional area, increased the total mechanism mass from 25.37 (kg) to 27.34 (kg). Although this represents a relative mass increment of 7.77%, it is justified by the substantial 581.8% improvement in the minimum safety factor, which rose from a critical failure state of 0.22 to a target value of 1.5. Given the typical payload capacities of eVTOL vehicles, this mass penalty of approximately 1.97 (kg) is considered acceptable in exchange for ensuring the structural integrity under the considered loading condition of the propulsor support during high-solicitation flight phases. This quantitative analysis confirms that the final design achieves an optimal balance between meeting stringent aerospace safety regulations and maintaining the lightweight characteristics essential for UAM performance.

As a final remark, the structural verification presented in this work is based on linear elastic finite element analysis under a critical static load. This approach is suitable for preliminary sizing and comparative evaluation of load-transfer strategies, but it does not replace a complete durability or certification-level assessment. In particular, the present analysis does not include nonlinear contact, local clearance effects, wear, fretting, fatigue damage accumulation, manufacturing tolerances, or cyclic load spectra. Moreover, the pin verification is based primarily on Von Mises stress and safety factor, whereas a complete joint design should also include bearing stress, shear-out resistance, hole-edge stress, pin-lug contact pressure, and fatigue checks. These aspects will be incorporated in the next stage of development, together with experimental validation on a physical prototype.

5. Summary, Conclusions, and Research Directions

5.1 Summary of the Issues Addressed in this Investigation

The evolution of the transport sector, along with the sustainability and ecological challenges it faces, requires innovative, unconventional, and functional engineering systems. Therefore, a viable solution explored in this study is to meet the need of creating a vehicle capable of air-to-ground transport. To achieve this goal, one of the main challenges is to design an opening mechanism that folds to reduce the overall footprint of the support system for propellers of flying vehicles, which is the main issue addressed in this investigation. The development of such a system poses several non-trivial engineering problems, including the kinematic and dynamic analysis of the deployable mechanism, the proper three-dimensional geometric design, and the final verification of the structural strength of the resulting design solution. In the present paper, this objective is achieved by cleverly leveraging the main areas of expertise of the authors, namely multibody dynamics, computational mechanics, system identification, and nonlinear control.

This paper addresses and resolves two significant issues of industrial and scientific interest: I) developing a deployment mechanism for a flying car and II) adopting a robust, systematic methodology for its mechanical design. For this purpose, particular attention is paid to the analysis of one of the most fundamental systems in flying cars, namely the motor support mechanism. In this vein, it is necessary to develop a new deployable mechanism with minimal space requirements during ground operation, enabled by folding into a relatively limited space. The design of such a system requires adopting an efficient, well-structured methodological process. To ensure reliability, an integrated CAD-MBD-FEM methodology is, therefore, adopted throughout this study, and the main aspects of this innovative workflow are demonstrated in the paper.

5.2 Discussion and Considerations on the Work Conducted

This paper presents the design of a deployable opening mechanism that supports the engines attached to the propellers of a flying car and folds during ground transport, thereby reducing the vehicle's overall size. To this end, an Integration of Computer-Aided Design and Analysis (I-CAD-A) approach is adopted throughout this investigation. In particular, the design and analysis methodology proposed in this work is based on a four-pillar framework: a) preliminary 2D modeling for system pre-dimensioning; b) detailed Computer-Aided Design (CAD) for 3D geometric modeling; c) Multi-Body Dynamic (MBD) analysis to identify the most severe loading conditions; and d) Finite Element Analysis (FEA) for final structural integrity verification. In this vein, the preliminary 2D design defines the kinematics of the deployable system and its maximum dimensions, providing the foundation for the subsequent development of the 3D CAD model. The geometry developed during the geometric modeling phase is also used to create the MBD model for kinematic synthesis and dynamic analysis, from which all reaction forces and moments at the joints are calculated and applied as external loads in the structural analysis. These applied loads are then carefully analyzed and transformed into an equivalent set of external forces and mechanical moments, since they cannot be directly transferred to the FEM environment for strength analysis. For this purpose, three new methods are introduced and analyzed in this paper, namely the Direct Reactions Method (DRM), the Moments Transformation Method (MTM), and the Loads Distribution Method (LDM). Finally, structural verification is performed using finite element analysis with the previously defined equivalent loading scenario. Several numerical experiments conducted in this investigation demonstrate that the proposed integrated approach yields a robust design.

For clarity, all steps for applying the integrated CAD-MBD-FEA methodology developed in this research are illustrated in the paper. The process starts with 3D modeling in a CAD environment to define the geometry of the system and ensure data transfers correctly to the MBD modeling stage. Then, multibody dynamic analysis allows for evaluating the constraint reactions at mechanical joints, which are then used as loads in the FEM analysis. In particular, special attention is given to the procedure for combining MBD and FEM modeling, since the reaction forces and moments obtained with MBD tools cannot be directly used in FEA for structural integrity verification. In fact, it is essential to note that incorrect load transfer between the MBD and FEA environments leads to inaccurate mechanical behavior assessment, resulting in an oversized system design. To solve this problem, three methods of load transfer are proposed and described in the paper, each highlighting potential advantages and weaknesses. These are 1) the Direct Reactions Method (DRM), 2) the Moments Transformation Method (MTM), and 3) the Loads Distribution Method (LDM). Through proper transfer and the iterative process shown in the paper, it is possible to define the minimum dimensions of each mechanical component to ensure the deployable system functions correctly. By doing so, the numerical analysis presented in this investigation demonstrates that the Loads Distribution Method (LDM) yields the most realistic structural results.

This investigation presents the conception and design of a complex mechanism using the integration of advanced mechanical methodologies. Based on the initial system dimensioning results, the CAD-MBD-FEM methodology utilized in this study enabled the definition of the actual system geometry for its mechanical design. In summary, the results presented in this study demonstrate the effectiveness of the CAD-MBD-FEM integrated approach in supporting the development of innovative mechanical systems. More importantly, the workflow described in the paper significantly reduces the risk of design errors and enables iterative refinement of system geometry. Furthermore, the proposed procedure provides guidance for designers working on complex mechanisms under variable load conditions. The proposed approach also offers greater accuracy and helps decrease the time and costs of subsequent validation and optimization phases. In conclusion, this investigation revealed that, among the methodologies considered, the most realistic is the one that converts constraint reaction forces into distributed loads and constraint reaction moments into distributed shear loads, namely the proposed technique referred to as the Loads Distribution Method (LDM). Future experimental validation using physical demonstrators will also need to account for typical aerospace manufacturing tolerances and potential surface defects. Assessing how these real-world manufacturing deviations affect the idealized load and stress distributions computed by the LDM will be crucial to the digital twin's final certification.

It is worth emphasizing that the structural verification in this study was conducted as a series of static analyses rather than a fully transient dynamic Finite Element Analysis (FEA). As detailed in the manuscript, the methodology involves identifying peak operational loads from dynamic simulations performed with the Multibody Dynamics (MBD) solver, which inherently accounts for the mechanism's global inertial effects and accelerations, and applying these worst-case loads to the structural components in a static FEA environment. Given the relatively slow, controlled deployment speeds of the support mechanism, potential inertial effects within the flexible components themselves during folding are considered secondary in this preliminary design phase. In effect, the local inertial forces generated by the mass of the individual links are significantly lower than the primary aerodynamic and structural loads transmitted through the joints. Consequently, focusing on static peak-load configurations provides a conservative and computationally efficient assessment of structural safety margins. This approach is consistent with the main scope of this investigation, which aims to achieve virtual prototyping of the folding mechanism under consideration as the case study. This research, therefore, provides a reliable baseline for the mechanism's feasibility before proceeding to more complex aeroelastic or flexible-body transient simulations in future design iterations.

5.3 Final Remarks and Future Developments

Although the methodology employed in this paper has proven effective for the case study of this investigation, namely the deployable mechanism that allows the motor support system of a flying car to open and fold, future developments will include implementing optimization algorithms to automate the search for optimal configurations of articulated mechanical systems in general. For instance, an important mechanical system that will be analyzed in future work adopting the integrated methodology devised in this paper is the mechanical transmission and governing system of the main rotor of a helicopter. In this context, adopting Design of Experiments (DOE) techniques will enable a systematic analysis of the influence of the key design parameters for the mechanical system under study. Furthermore, the use of machine learning-based approaches enables the generation of an optimized geometry that focuses on structural stiffness and strength. Overall, this work advances the integration of design and analysis methodologies applicable to any articulated system that can be described within the framework of multibody mechanical systems.

Future work will focus on strengthening the Integration of Computer-Aided Design and Analysis (I-CAD-A) by establishing a bidirectional CAD-CAE digital thread that ensures geometry, materials, boundary conditions, and load histories remain consistent and traceable across design iterations. Additionally, the I-CAD-A workflow will be extended to include optimization and verification, combining multi-fidelity simulations with targeted experimental correlation to quantify predictive accuracy and support design decisions for rigid-flexible multibody mechanical systems. Finally, the key features and performance of the Loads Distribution Method (LDM) will be further analyzed to enhance and advance the technique for accurately converting the mechanical actions resulting from rigid dynamic models to static structural models.

While the current design meets the rigorous safety-factor requirements established by aviation standards, the structural architecture offers significant opportunities for mass optimization. The results presented in this study are intended to provide a robust, validated baseline, confirming that the integrated CAD-MBD-FEM framework reliably predicts the mechanical behavior of the complex foldable mechanism. Building on this foundation, future research cycles will prioritize lightweighting strategies to enhance the vehicle's operational efficiency and payload capacity. Specifically, subsequent phases will apply topology optimization and generative design algorithms to the primary structural components, enabling the strategic removal of material in low-stress regions while maintaining the required stiffness. Additionally, the transition from traditional alloy steels to advanced high-modulus carbon fiber composites, as well as the adoption of additive manufacturing techniques, will be explored. These optimization directions will ensure that the final iteration of the deployable support not only meets the necessary structural safety margins but also achieves the high strength-to-weight ratio essential for the competitive UAM market.

Regarding the structural validation of the mechanism, the LDM, while numerically superior at capturing realistic stress gradients, requires subsequent empirical verification to confirm its underlying assumptions. To address this limitation, the next phase of this research will develop a dedicated physical test bench for the foldable mechanism. This experimental campaign will prioritize validating the surface-pressure assumptions used in the LDM by using thin-film pressure sensors and miniature strain gauges strategically embedded at the joint interfaces. Furthermore, Digital Image Correlation (DIC) will be used to map the full-field strain distribution on the structural arms, enabling a direct quantitative comparison between the physical deformation and the FEM results. These experiments will provide the necessary benchmark data to calibrate the pressure distribution profiles within the I-CAD-A framework, ensuring that the virtual prototyping methodology accurately reflects the complex contact mechanics of the physical aerospace component. This empirical correlation is essential for bridging the gap between the current high-fidelity simulations and the rigorous safety requirements of the UAM industry.

In the proposed design, transitioning the structural arms from high-strength metallic alloys to Carbon Fiber-Reinforced Polymers (CFRP) will introduce significant modeling challenges that the I-CAD-A framework must address in future work [108]. Primarily, the computational core will need to shift from assuming isotropic material behavior to accounting for the orthotropic nature of composite laminates, which requires a detailed, layer-by-layer constitutive definition. In critical load-transfer regions, such as pin joints and bonded interfaces, the current assumptions of simple metallic contact will be insufficient. Future developments will therefore require the integration of Cohesive Zone Modeling (CZM) to accurately simulate the initiation and progression of delamination in glued joints [109]. Moreover, the structural validation loop will be updated to incorporate specialized failure criteria, such as the Tsai-Wu or Hashin theories, to account for the distinct failure modes of fibers and matrix [110]. This evolution of the virtual prototyping environment will be essential to ensuring the reliability of the lightweight, high-performance composite architectures required for advanced UAM vehicles.

Author Contributions

This paper was principally devised and developed by the first author (Carlos Pérez Carrera) and by the second author (Rosario La Regina). Great support in the development of the research was provided by the third author (Carmine Maria Pappalardo) and by the fourth author (Valentino Paolo Berardi). The detailed review carried out by the fifth author (Domenico Guida) considerably improved the quality of the work. The manuscript was written with substantial contributions from all authors. All authors reviewed the methodology, discussed the results, revised the paper content, and approved the final manuscript version.

Acknowledgments

Not applicable.

Conflict of Interest

The authors declared no potential conflicts of interest with respect to the research, authorship, and publication of this article.

Funding

The authors received no financial support for the research, authorship, and publication of this article.

Data Availability Statements

The datasets generated and/or analyzed during the current study are available from the corresponding author on reasonable request.

References

[1] Ahmed, S.S., Hulme, K.F., Fountas, G., Eker, U., Benedyk, I.V., Still, S.E., Anastasopoulos, P.C., The flying car—challenges and strategies toward future adoption, *Frontiers in Built Environment*, 6, 2020, 106.
[2] Yang, C., Lu, Z., Wang, W., Li, Y., Chen, Y., Xu, B., Energy management of hybrid electric propulsion system: Recent progress and a flying car perspective under three-dimensional transportation networks, *Green Energy and Intelligent Transportation*, 2(1), 2023, 100061.
[3] Ahmed, S.S., Fountas, G., Eker, U., Still, S.E., Anastasopoulos, P.C., An exploratory empirical analysis of willingness to hire and pay for flying taxis and shared flying car services, *Journal of Air Transport Management*, 90, 2021, 101963.
[4] Aláez, D., Olaz, X., Prieto, M., Villadangos, J., Astrain, J.J., Vtol uav digital twin for take-off, hovering and landing in different wind conditions, *Simulation Modelling Practice and Theory*, 123, 2023, 102703.
[5] Pukhova, A., Llorca, C., Moreno, A., Staves, C., Zhang, Q., Moeckel, R., Flying taxis revived: Can urban air mobility reduce road congestion?, *Journal of Urban Mobility*, 1, 2021, 100002.
[6] Stopher, P.R., Reducing road congestion: a reality check, *Transport policy*, 11(2), 2004, 117–131.
[7] Duranton, G., Turner, M.A., The fundamental law of road congestion: Evidence from us cities, *American Economic Review*, 101(6), 2011, 2616–2652.
[8] Padrón, J.D., Hernández-Orallo, E., Calafate, C.T., Soler, D., Cano, J.C., Manzoni, P., Realistic traffic model for urban environments based on induction loop data, *Simulation modelling practice and theory*, 125, 2023, 102742.
[9] Yan, Y., Wang, K., Qu, X., Urban air mobility (uam) and ground transportation integration: A survey, *Frontiers of Engineering Management*, 11(4), 2024, 734–758.
[10] Pan, G., Alouini, M.S., Flying car transportation system: Advances, techniques, and challenges, *IEEE Access*, 9, 2021, 24586–24603.
[11] Choudhary, C., Aastha, Saini, G.K., Kunal, Saxena, M., Evaluation of potential flying cars, *2023 2nd International Conference for Innovation in Technology (INOCON)*, 1–5.
[12] Bando, M., Hasebe, K., Nakayama, A., Shibata, A., Sugiyama, Y., Dynamical model of traffic congestion and numerical simulation, *Physical review E*, 51(2), 1995, 1035.
[13] Arnott, R., Rave, T., Schöb, R., Alleviating urban traffic congestion, *MIT Press Books*, 1, 2005.
[14] Postorino, M.N., Sarné, G.M., Reinventing mobility paradigms: Flying car scenarios and challenges for urban mobility, *Sustainability*, 12(9), 2020, 3581.

[15] Marzouk, O.A., Urban air mobility and flying cars: Overview, examples, prospects, drawbacks, and solutions, *Open Engineering*, 12(1), 2022, 662–679.
[16] Evans, L., Frick, M.C., Schwing, R.C., Is it safer to fly or drive?, *Risk Analysis*, 10(2), 1990, 239–246.
[17] Rajashekara, K., Wang, Q., Matsuse, K., Flying cars: Challenges and propulsion strategies, *IEEE Electrification Magazine*, 4(1), 2016, 46–57.
[18] Shi, X., Kim, K., Rahili, S., Chung, S.J., Nonlinear control of autonomous flying cars with wings and distributed electric propulsion, *2018 IEEE Conference on Decision and Control (CDC)*, 5326–5333.
[19] Kasliwal, A., Furbush, N.J., Gawron, J.H., McBride, J.R., Wallington, T.J., De Kleine, R.D., Kim, H.C., Keoleian, G.A., Role of flying cars in sustainable mobility, *Nature communications*, 10(1), 2019, 1555.
[20] Bashir, N., Boudjit, S., Dauphin, G., Zeadally, S., An obstacle avoidance approach for uav path planning, *Simulation modelling practice and theory*, 129, 2023, 102815.
[21] Zohdi, T., On the dynamics and breakup of quadcopters using a discrete element method framework, *Computer Methods in Applied Mechanics and Engineering*, 327, 2017, 503–521.
[22] Al-Madani, B., Svirskis, M., Narvydas, G., Maskeliunas, R., Damasevicius, R., Design of fully automatic drone parachute system with temperature compensation mechanism for civilian and military applications, *Journal of Advanced Transportation*, 2018(1), 2018, 2964583.
[23] Xu, D., Hui, Z., Liu, Y., Chen, G., Morphing control of a new bionic morphing uav with deep reinforcement learning, *Aerospace science and technology*, 92, 2019, 232–243.
[24] Marano, D., Cammarata, A., Fichera, G., Sinatra, R., Prati, D., Modeling of a three-axes mems gyroscope with feedforward pi quadrature compensation, *Advances on Mechanics, Design Engineering and Manufacturing: Proceedings of the International Joint Conference on Mechanics, Design Engineering & Advanced Manufacturing (JCM 2016), 14-16 September, 2016, Catania, Italy*, Springer, 71–80.
[25] Hu, L., Yan, X., Yuan, Y., Development and challenges of autonomous electric vertical take-off and landing aircraft, *Heliyon*, 11(1), 2025.
[26] Bustos, A., Rubio, H., Soriano-Heras, E., Castejon, C., Methodology for the integration of a high-speed train in maintenance 4.0, *Journal of Computational Design and Engineering*, 8(6), 2021, 1605–1621.
[27] Wilkinson, T.L., Load distribution among bolts parallel to load, *Journal of structural engineering*, 112(4), 1986, 835–852.
[28] Li, C.C., Doucet, C., Performance of d-bolts under dynamic loading, *Rock mechanics and rock engineering*, 45(2), 2012, 193–204.
[29] Nikravesh, S.M.Y., Goudarzi, M., A review paper on looseness detection methods in bolted structures, *Latin American Journal of Solids and Structures*, 14(12), 2017, 2153–2176.
[30] Bickford, J., *Handbook of Bolts and bolted Joints*, MarcelDekker, 1998.
[31] Vlase, S., Marin, M., Iuliu, N., Finite element method-based elastic analysis of multibody systems: a review, *Mathematics*, 10(2), 2022, 257.
[32] Widiyanto, I., Sutimin, S., Laksono, F.B., Prabowo, A.R., Structural assessment of monocoque frame construction using finite element analysis: A study case on a designed vehicle chassis referring to ford gt40, *Procedia Structural Integrity*, 33, 2021, 27–34.
[33] Lee, S.H., A cad–cae integration approach using feature-based multi-resolution and multi-abstraction modelling techniques, *Computer-Aided Design*, 37(9), 2005, 941–955.
[34] Pappalardo, C.M., Lettieri, A., Guida, D., Identification of a dynamical model of the latching mechanism of an aircraft hatch door using the numerical algorithms for subspace state-space system identification, *IAENG International Journal of Applied Mathematics*, 51(2), 2021, 1–14.
[35] Pappalardo, C.M., Manca, A.G., Guida, D., A combined use of the multibody system approach and the finite element analysis for the structural redesign and the topology optimization of the latching component of an aircraft hatch door., *IAENG International Journal of Applied Mathematics*, 51(1), 2021.
[36] Zhang, H., Wang, L., Liu, Y., A hybrid model-based and data-driven method for mechanical-thermal dynamic load identification considering multi-source uncertainties, *Computer Methods in Applied Mechanics and Engineering*, 435, 2025, 117662.
[37] Pappalardo, C.M., Curcio, M., Guida, D., Modeling the longitudinal flight dynamics of a fixed-wing aircraft by using a multibody system approach., *IAENG International Journal of Computer Science*, 50(1), 2023.
[38] Eker, U., Ahmed, S.S., Fountas, G., Anastasopoulos, P.C., An exploratory investigation of public perceptions towards safety and security from the future use of flying cars in the united states, *Analytic methods in accident research*, 23, 2019, 100103.
[39] Pérez Carrera, C., Genel, Ö.E., La Regina, R., Pappalardo, C.M., Guida, D., A comprehensive and systematic literature review on flying cars in contemporary research, *Journal of Applied and Computational Mechanics*, 11(3), 2025, 642–666.
[40] Sorgonà, O., Cirelli, M., Giannini, O., Verotti, M., Comparison of flexibility models for the multibody simulation of compliant mechanisms, *Multibody System Dynamics*, 63(3), 2025, 453–474.
[41] Gao, F., Li, J., Sun, G., Efficient and accurate flexible multibody dynamics modeling for complex spacecraft with integrated control applications, *Acta Astronautica*, 219, 2024, 818–825.
[42] Ortiz, M., Leroy, Y., Needleman, A., A finite element method for localized failure analysis, *Computer methods in applied mechanics and engineering*, 61(2), 1987, 189–214.
[43] Ardila-Parra, S.A., Pappalardo, C.M., Estrada, O.A.G., Guida, D., Finite element based redesign and optimization of aircraft structural components using composite materials, *IAENG International Journal of Applied Mathematics*, 50(4), 2020.
[44] Sarcar, M., Rao, K.M., Narayan, K.L., *Computer aided design and manufacturing*, PHI Learning Pvt. Ltd., 2008.
[45] Chen, F., Mac, G., Gupta, N., Security features embedded in computer aided design (cad) solid models for additive manufacturing, *Materials & Design*, 128, 2017, 182–194.
[46] Bandler, J.W., Optimization methods for computer-aided design, *IEEE Transactions on Microwave Theory and Techniques*, 17(8), 1969, 533–552.
[47] Fontana, C., Cappetti, N., Three-dimensional reconstruction of the right ventricle from a radial basis morphing of the inner surface, *Computation*, 12(11), 2024, 216.
[48] Pérez Bayas, M.A., Cely, J., Sintov, A., García Cena, C.E., Saltaren, R., Method to develop legs for underwater robots: From multibody dynamics with experimental data to mechatronic implementation, *Sensors*, 22(21), 2022.
[49] Kennard, R.W., Stone, L.A., Computer aided design of experiments, *Technometrics*, 11(1), 1969, 137–148.
[50] Louhichi, B., Abenhaim, G.N., Tahan, A.S., Cad/cae integration: updating the cad model after a fem analysis, *The International Journal of Advanced Manufacturing Technology*, 76(1), 2015, 391–400.
[51] Chiu, W., Tan, S., Multiple material objects: from cad representation to data format for rapid prototyping, *Computer-Aided Design*, 32(12), 2000, 707–717.
[52] Schutte, A., Udwadia, F., New approach to the modeling of complex multibody dynamical systems, *Journal of Applied Mechanics*, 78(2), 2010, 021018.
[53] Kim, H., Lee, H., Lee, K., Cho, H., and, M.C., Efficient flexible multibody dynamic analysis via improved c0 absolute nodal coordinate formulation-based element, *Mechanics of Advanced Materials and Structures*, 29(25), 2022, 4125–4137.
[54] Zhou, Z., Xu, Y., and, G.X., Dynamics for rigid–flexible coupled solar panel multibody system composed of composite laminated plates, *Mechanics of Advanced Materials and Structures*, 0(0), 2024, 1–15.
[55] Cammarata, A., Maddio, P.D., Sinatra, R., Tian, Y., Zhao, Y., Xi, F., Elastostatic analysis of a module-based shape morphing snake-like robot, *Mechanism and Machine Theory*, 194, 2024, 105580.
[56] Dietz, S., Netter, H., Sachau, D., Fatigue life predictions by coupling finite element and multibody systems calculations, *Proceedings of the ASME 1997 Design Engineering Technical Conferences*, 1–9, paper No. DETC97/VIB-4229.
[57] Braccesi, C., Cianetti, F., Landi, L., Random loads fatigue: The use of spectral methods within multibody simulation, *Proceedings of the ASME 2005 International Design Engineering Technical Conferences*, 1735–1745.
[58] Giesbers, J., Contact mechanics in msc adams - a technical evaluation of the contact models in multibody dynamics software msc adams, 2012.
[59] Schuderer, M., Rill, G., Schaeffer, T., Schulz, C., Friction modeling from a practical point of view, *Multibody System Dynamics*, 63(1), 2025, 141–158.
[60] Cammarata, A., Sinatra, R., Rigato, R., Maddio, P.D., Tie-system calibration for the experimental setup of large deployable reflectors, *Machines*, 7(2), 2019, 23.
[61] Dhatt, G., Lefrançois, E., Touzot, G., *Finite element method*, John Wiley & Sons, 2012.
[62] Bouzidi, I., Hadjoui, A., and, A.F., Dynamic analysis of functionally graded rotor-blade system using the classical version of the finite element method, *Mechanics Based Design of Structures and Machines*, 49(7), 2021, 1080–1108.
[63] Akgun, F., A finite element model for analyzing horizontal well bha behavior, *Journal of Petroleum Science and Engineering*, 42(2), 2004, 121–132, petroleum Exploration and Production Research in the Middle East.

[64] Pappalardo, C.M., Magaldi, T., Masucci, L., La Regina, R., Naddeo, A., Virtual prototyping, multibody dynamics, and control design of an adaptive lift table for material handling, *Journal of Applied and Computational Mechanics*, 10(4), 2024, 659–693.
[65] Louhichi, B., Aifaoui, N., Hamdi, M., Abdelmajid, B., An optimization-based computational method for surface fitting to update the geometric information of an existing b-rep cad..., *International Journal of CAD/CAM*, 9(1), 2009, 17–24.
[66] Hamed, A.M., Jayakumar, P., Letherwood, M.D., Gorsich, D.J., Recuero, A.M., Shabana, A.A., Ideal Compliant Joints and Integration of Computer Aided Design and Analysis, *Journal of Computational and Nonlinear Dynamics*, 10(2), 2015, 021015.
[67] Wu, D., Zheng, A., Yu, W., Cao, H., Ling, Q., Liu, J., Zhou, D., Digital twin technology in transportation infrastructure: a comprehensive survey of current applications, challenges, and future directions, *Applied Sciences*, 15(4), 2025, 1911.
[68] De Simone, M.C., Veneziano, S., Porcaro, A., Guida, D., Design of experiments approach for structural optimization of urban air mobility vehicles, *Actuators*, 14, 2025, 176.
[69] Foucault, G., Cuillière, J.C., François, V., Léon, J.C., Maranzana, R., Adaptation of cad model topology for finite element analysis, *Computer-Aided Design*, 40(2), 2008, 176–196.
[70] Stolt, R., A cad-integrated system for automated idealization of cad-models for finite element analysis, *International Design Engineering Technical Conferences and Computers and Information in Engineering Conference*, vol. 4739, 457–466.
[71] GCR, N., Cost analysis of inadequate interoperability in the us capital facilities industry, *National Institute of Standards and Technology (NIST)*, 2004, 223–253.
[72] Cottrell, J.A., Hughes, T.J., Bazilevs, Y., *Isogeometric analysis: toward integration of CAD and FEA*, John Wiley & Sons, 2009.
[73] Ji, A.M., Zhu, K., Huang, J.C., Dong, Y.P., Cad/cae integration system of mechanical parts, *Advanced Materials Research*, 338, 2011, 272–276.
[74] Mounir, H., Nizar, A., Abdelmajid, B., Cad model simplification using a removing details and merging faces technique for a fem simulation, *Journal of mechanical science and technology*, 26(11), 2012, 3539–3548.
[75] Tierney, C., Nolan, D., Robinson, T., Armstrong, C., Using mesh-geometry relationships to transfer analysis models between cae tools, *Engineering with Computers*, 31(3), 2015, 465–481.
[76] Hamed, A.M., Jayakumar, P., Letherwood, M.D., Gorsich, D.J., Recuero, A.M., Shabana, A.A., Ideal compliant joints and integration of computer aided design and analysis, *Journal of Computational and Nonlinear Dynamics*, 10(2), 2015, 021015.
[77] Lian, H., Bordas, S., Sevilla, R., Simpson, R., Recent developments in cad/analysis integration, *arXiv preprint arXiv:1210.8216*, 2012.
[78] Bayas, M.P., Andrade, G.N., Arroba, S.M.A., Carrión, J.G., Kinetic analysis of an ankle rehabilitator composed of two parallel delta robots, *Proceedings of CLAWAR 2018: 21st International Conference on Climbing and Walking Robots and the Support Technologies for Mobile Machines*, 89–97.
[79] Braccesi, C., Landi, L., Scaletta, R., New dual meshless flexible body methodology for multi-body dynamics: Simulation of generalized moving loads, *Proceedings of The Institution of Mechanical Engineers Part K-journal of Multi-body Dynamics - PROC INST MECH ENG K-J MUL D*, 218, 2004, 51–62.
[80] Villecco, F., On the evaluation of errors in the virtual design of mechanical systems, *Machines*, 6(3), 2018, 36.
[81] Kashem, M.A., Shamsuddoha, M., Nasir, T., Sustainable transportation solutions for intelligent mobility: A focus on renewable energy and technological advancements for electric vehicles (evs) and flying cars, *Future Transportation*, 4(3), 2024, 874–890.
[82] Arabshahi, S., Barton, D., Shaw, N., Steps towards cad-fea integration, *Engineering with Computers*, 9(1), 1993, 17–26.
[83] Sanborn, G.G., Shabana, A.A., On the integration of computer aided design and analysis using the finite element absolute nodal coordinate formulation, *Multibody System Dynamics*, 22(2), 2009, 181–197.
[84] Zhang, L., Le, B., Akhtar, N., Lam, S.K., Ngo, D., Large language models for computer-aided design: A survey, *ACM Computing Surveys*, 58(9), 2026, 1–39.
[85] Cuillière, J.C., Francois, V., Integration of cad, fea and topology optimization through a unified topological model, *Computer-Aided Design and Applications*, 11(5), 2014, 493–508.
[86] Perrella, M., Armentani, E., Lamanna, G., Berardi, V.P., Effect of fracture energy estimation on the predictions of mode ii behavior of bonded joints using cohesive zone models, *Fracture and Structural Integrity*, 19(72), 2025, 236–246.
[87] Cricrì, G., Perrella, M., Berardi, V.P., Identification of cohesive zone model parameters based on interface layer displacement field of bonded joints, *Fatigue & Fracture of Engineering Materials & Structures*, 45(3), 2022, 821–833.
[88] Perrella, M., Berardi, V., Cricrì, G., A novel methodology for shear cohesive law identification of bonded reinforcements, *Composites Part B: Engineering*, 144, 2018, 126–133.
[89] Saxena, A., Sahay, B., *Computer Aided Engineering Design*, Springer, New York, NY, 2005th ed., 2005.
[90] Piegl, L., Tiller, W., *The NURBS Book*, Monographs in Visual Communication, Springer, Berlin, Germany, 2nd ed., 1996.
[91] Shabana, A.A., *Dynamics of multibody systems*, Cambridge university press, 2020.
[92] Pappalardo, C.M., Guida, D., On the computational methods for solving the differential-algebraic equations of motion of multibody systems, *Machines*, 6(2), 2018, 20.
[93] Zienkiewicz, O.C., Taylor, R.L., Zhu, J.Z., *The finite element method: Its basis and fundamentals*, The Finite Element Method, Butterworth-Heinemann, Oxford, England, 7th ed., 2013.
[94] Rao, S.S., *The finite element method in engineering*, Elsevier, 2010.
[95] Li, S., Shen, Y., Liu, B., Chao, X., He, S., Feng, G., Aerodynamic design and analysis of an aerial vehicle module for split-type flying cars in urban transportation, *Aerospace*, 12(10), 2025, 871.
[96] Shao, H., Kan, Z., Wang, Y., Li, D., Yao, Z., Xiang, J., Dynamic analysis and numerical simulation of arresting hook engaging cable in carried-based uav landing process, *Drones*, 7(8), 2023, 530.
[97] Xie, A., Yan, X., Liang, W., Zhu, S., Chen, Z., Large-sized multirotor design: Accurate modeling with aerodynamics and optimization for rotor tilt angle, *Drones*, 7(10), 2023, 614.
[98] Zhang, T., Grzelak, D., Zhao, W., Islam, M.A., Fricke, H., Assmann, U., A review on the construction, modeling, and consistency of digital twins for advanced air mobility applications, *Drones*, 9(6), 2025, 394.
[99] Villecco, F., Pellegrino, A., Evaluation of uncertainties in the design process of complex mechanical systems, *Entropy*, 19(9), 2017, 475.
[100] XPENG, Xpeng x2 completes first global public flight in dubai, 2022, official company news release.
[101] Federal Aviation Administration, 14 CFR § 27.303 – Factor of Safety, 2026, electronic Code of Federal Regulations, Alternate reference: FAR 27.303, Accessed: 2026-05-13.
[102] Bickford, J.H., *Introduction to the Design and Behavior of Bolted Joints: Non-Gasketed Joints*, CRC Press, 4th ed., 2007.
[103] Lurie, A.I., *Theory of elasticity*, Springer Science & Business Media, 2010.
[104] Virgamet, 38hn3m, 39nicrmo3, 1.6510, 38ncd4, 39nicrmos3, 38nicrmo4 alloy steel, 2024, accessed: 20-Oct-2024.
[105] Williams, M., *Structures: theory and analysis*, Bloomsbury Publishing, 2020.
[106] MatWeb, Aluminum 7075-t6, 2024, available online at https://www.matweb.com, datasheet for Aluminum 7075-T6, accessed 20 Oct 2024.
[107] MathWorks, Simscape multibody, 2024, available online: https://es.mathworks.com/products/simscape-multibody.html, accessed 20 Oct 2024.
[108] Davidson, M., Graunke, R., Green, A., Haelsig, H., Heinemann, L., Antony Jose, S., Menezes, P.L., Carbon fiber-reinforced polymer matrix composites: Processing, properties, and applications, *Fibers*, 14(3), 2026, 29.
[109] Zhu, Y., Zhang, Y., Xiang, L., Crack propagation behavior modeling of bonding interface in composite materials based on cohesive zone method, *Buildings*, 15(10), 2025, 1717.
[110] Alnomani, S.N., Hunain, M.B., Alhumairee, S.H., Investigation of different failure theories for a lamina of carbon fiber/epoxy matrix composite materials, *Journal of Engineering Science and Technology*, 15(2), 2020, 846–857.

ORCID iD

Carlos Pérez Carrera https://orcid.org/0009-0006-8946-4195
Rosario La Regina https://orcid.org/0000-0003-4934-5678
Carmine Maria Pappalardo https://orcid.org/0000-0003-3763-7104
Valentino Paolo Berardi https://orcid.org/0000-0002-0008-4828

Domenico Guida https://orcid.org/0000-0002-2870-9199

How to cite this article: Carlos Pérez Carrera, Rosario La Regina, Carmine Maria Pappalardo, Valentino Paolo Berardi, Domenico Guida. An Integrated CAD-MBD-FEM Framework for Virtual Prototyping of a New Foldable Mechanism for Deployable Propulsor Support in Urban Air Mobility Vehicles, J. Appl. Comput. Mech., xx(x), 2026, 1-34. https://doi.org/10.22055/jacm.2026.49210.5807